

# Experimental and Theoretical Assessments of Aluminum Proximity in MFI Zeolites and Its Alteration by Organic and Inorganic Structure-Directing Agents

Claire T. Nimlos,<sup>§</sup> Alexander J. Hoffman,<sup>§</sup> Young Gul Hur, Byung Jin Lee, John R. Di Iorio, David D. Hibbitts,\* and Rajamani Gounder\*

Cite This: <https://dx.doi.org/10.1021/acs.chemmater.0c03154>

Read Online

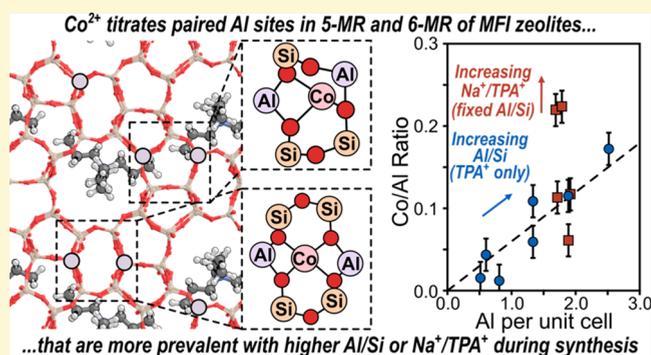
ACCESS |

Metrics & More

Article Recommendations

Supporting Information

**ABSTRACT:** The molecular structure and cationic charge density of organic and inorganic structure-directing agents (SDAs) influence the siting and arrangement of Al substituted in zeolite frameworks. Yet, developing robust synthesis–structure relations for MFI zeolites is difficult because of the complexities inherent to its low-symmetry framework (12 unique tetrahedral sites), which generates a large combinatorial space of Al–Al site pairs to exhaustively model by density functional theory (DFT) and quantify by experiment. Here, we develop an experimental protocol to reproducibly quantify  $\text{Co}^{2+}$ -titratable Al–Al site pairs in MFI with saturation uptakes validated by corroborating spectroscopic and cation site balance data. Using tetrapropylammonium ( $\text{TPA}^+$ ) as the sole SDA, MFI zeolites were crystallized with varying Al contents ( $\text{Si}/\text{Al} = 37\text{--}185$ ; 0.52–2.52 Al per unit cell) within a composition range consistent with charge density mismatch theory and the occlusion of one  $\text{TPA}^+$  per channel intersection with fractions of paired Al (0.0–0.34) that increased with bulk Al content. DFT calculations performed using a 96 T-site MFI unit cell containing either an isolated Al site (all 96 configurations) or various Al–Al site pairs (1773 out of 13 680 total configurations), charge balanced by one or two  $\text{TPA}^+$ , respectively, reveal the dominant influence of electrostatic interactions between the cationic N of  $\text{TPA}^+$  and the anionic lattice charge on Al siting energies. Together with DFT calculations of  $\text{Co}^{2+}$  exchange energies at Al–Al site pairs, theory predicts that two  $\text{TPA}^+$  cations confined within adjacent channel intersections can form many Al–Al site pair ensembles that are  $\text{Co}^{2+}$ -titratable, rationalizing the considerable presence of paired Al sites in MFI samples crystallized using only  $\text{TPA}^+$ . The use of  $\text{TPA}^+$  and  $\text{Na}^+$  as co-SDAs in the synthesis gel, while varying the  $\text{Na}^+/\text{TPA}^+$  ratio (0–5) at a constant SDA/Al ratio ( $(\text{TPA}^+ + \text{Na}^+)/\text{Al} = 30$ ), crystallized MFI with a similar bulk Al content ( $\text{Si}/\text{Al} \approx 50$ ) but varying fractions of Al in pairs (0.12–0.44). Separate crystallization experiments performed using charge-neutral organic SDAs, either pentaerythritol or a mixture of 1,4-diazabicyclo[2.2.2]octane and methylamine, together with  $\text{Na}^+$  to compensate for framework Al, crystallized MFI at similar bulk Al content ( $\text{Si}/\text{Al} \approx 50$ ) but with lower fractions of Al in pairs (<0.14). Among MFI samples crystallized with an organic SDA and  $\text{Na}^+$  as a co-SDA, the number of paired Al sites formed generally increased with the co-occluded  $\text{Na}^+$  content on the zeolite, a synthesis–structure relation that resembles our prior observations on CHA zeolites. The combined theoretical and experimental approach used here provides a microscopic model to define and quantify Al–Al site pairs in MFI, which can be adapted to do so for other framework topologies. These findings highlight how such Al siting models can be exercised to quantitatively characterize zeolite materials to develop synthetic strategies that can predictably vary their framework Al arrangements and catalytic and adsorption properties in turn, as shown here for samples of essentially constant bulk composition by exploiting mixtures of organic and inorganic SDAs during hydrothermal crystallization.



## 1. INTRODUCTION

Zeolites are aluminosilicate molecular sieves that contain some fraction of their framework  $\text{Si}^{4+}$  substituted with  $\text{Al}^{3+}$ , which generates an anionic lattice charge ( $[\text{AlO}_{4/2}]^-$  tetrahedron; hereafter denoted  $\text{Al}^-$  as shorthand) capable of balancing various extraframework cationic species (e.g., protons) that can serve as catalytic active sites. The opportunity to position Al atoms in unique coordination environments and in turn to host

Received: July 31, 2020

Revised: October 2, 2020

cationic species and complexes within different void environments is dictated by the framework topology. In the case of the MFI framework topology, 12 crystallographically distinct tetrahedral sites (T-sites) and 26 unique framework O atoms ( $O_f$ ) are present in its orthorhombic crystal symmetry.<sup>1</sup> Cationic species can reside within the various (alumino)siloxane ring structures present (4-, 5-, 6-, 10-MR; “X-MR” denotes an X-membered ring) and within the larger microporous voids formed from the specific arrangement of these rings, generally classified by either straight or sinusoidal 10-MR channels that define the pore-limiting diameter ( $\sim 0.5$  nm) and channel intersections that define the largest cavity diameter ( $\sim 0.7$  nm).<sup>2</sup> A seminal study of H-MFI with varying bulk Al content ( $Si/Al = 15\text{--}10\,000$ ) by these authors reported *n*-hexane cracking rates (per gram) that increased linearly with total Al content (per gram), suggesting either that protons located at the 26 unique framework O are equally reactive<sup>3</sup> or that they possess site-specific reactivity but that the distribution of Al and protons among MFI samples of varying composition is invariant,<sup>4,5</sup> a possibility suggested originally by Haag and co-workers.<sup>6</sup> Subsequent studies have shown that turnover rates of Brønsted acid-catalyzed reactions (including alkane cracking<sup>5</sup>) differ for nominally isolated acid sites that are similar in acid strength (estimated by their deprotonation energy, or DPE)<sup>7</sup> but confined within different void environments to the extent that nonspecific van der Waals forces stabilize kinetically relevant transition states and precursors differently.<sup>5,8,9</sup>

Lattice Al atoms can also be present in close relative proximity, such as when two Al atoms are substituted in the same X-MR and separated by one or more Si atoms, given that Löwenstein’s rule dictates that Al substitution in the nearest-neighbor (NN) positions is prohibited.<sup>10</sup> Such proximal Al substitution patterns generate Brønsted acid sites that can alter acid strength<sup>11,12</sup> and have been shown to stabilize kinetically relevant alkanol dehydration transition states and precursors to different extents<sup>13</sup> via specific arrangements of hydrogen-bonding interactions among anionic lattice oxygen and cationic protons, adsorbates, and transition states. Proximal acid sites in MFI have been implicated to influence the catalytic rates of *n*-alkane cracking,<sup>14</sup> product distributions formed from alkene oligomerization<sup>15,16</sup> and alkane cracking,<sup>17,18</sup> and methanol clustering and reactivity as relevant for methanol to aromatics<sup>19</sup> and hydrocarbons<sup>20</sup> processes. Proximal lattice Al atoms have also long been recognized to influence the ability to exchange various types of extraframework metal ions and complexes that serve as precursor or active sites for oxidation, reduction, and decomposition reactions of nitrogen oxides (Cu,<sup>21–23</sup> Fe<sup>24–27</sup>), partial oxidation of methane (Cu,<sup>28,29</sup> Fe<sup>30,31</sup>), dehydrogenation of light alkanes (Ga),<sup>32–34</sup> dehydroaromatization of methane (Mo),<sup>35–37</sup> and aromatization of methanol (Zn).<sup>38</sup> In addition, different Al arrangements have also been linked to adsorption behavior (e.g., CO<sub>2</sub>,<sup>39</sup> alkanes,<sup>40</sup> water<sup>41</sup>) and hydrothermal stability.<sup>42–44</sup>

Despite this growing recognition that lattice Al proximity can influence the catalytic and adsorption behavior, the ability to synthesize MFI zeolites with well-defined Al distributions and systematic variations in their number of proximal Al sites is limited; generally accepted conclusions state that the Al arrangement in MFI depends on the synthesis conditions used (e.g., inorganic reagent sources,<sup>19,45</sup> structure-directing agents (SDAs)<sup>45–49</sup>) but in an apparently nonsystematic manner.<sup>50</sup>

Recently, we reported that the molecular structure and cationic charge density of the SDAs used to crystallize CHA zeolites influences Al proximity in 6-MRs in a predictable and systematic manner.<sup>51,52</sup> This conclusion was predicated on accurate experimental quantification of paired Al sites (two Al in a 6-MR) in CHA using a functional titrant (e.g., Co<sup>2+</sup>) in which NH<sub>3</sub> titration of residual H<sup>+</sup> sites on Co-form samples could be performed to determine a site balance that verified 2:1 H<sup>+</sup>:Co<sup>2+</sup> exchange and density functional theory (DFT) calculations to determine the preference of Co<sup>2+</sup> titrants to exchange at these specific Al–Al site pair ensembles. In contrast to CHA, efforts to develop synthetic strategies to systematically influence the Al proximity in MFI have been challenged by the ambiguity in identifying the microscopic Al–Al site ensembles referred to in colloquial descriptions of “proximity” given that its low-symmetry framework generates a large combinatorial space of Al–Al site ensembles to consider in computational models. Experimental efforts typically attempt to quantify “proximal” Al sites in MFI by aqueous-phase Co<sup>2+</sup> ion exchange, although ion-exchange protocols differ widely among research groups<sup>14,45,48,53–61</sup> and are typically performed at ambient temperature (ca. 298 K);<sup>14,45,53–55</sup> however, such ion-exchange protocols do not necessarily guarantee the saturation of all accessible Al–Al pairs in MFI, as we have shown recently requires ion exchange performed at elevated temperatures (353 K).<sup>58</sup> Co<sup>2+</sup> species on zeolites are commonly identified in diffuse reflectance UV–vis (DRUV) spectra (typically measured at ambient temperatures) with attempts often made to deconvolute Co<sup>2+</sup> d–d transition bands into different components purported to reflect distinct Co<sup>2+</sup> geometries resulting from coordination within distinct lattice binding sites (e.g.,  $\alpha$ ,  $\beta$ , and  $\gamma$  sites). Such interpretations are inaccurate, however, because even a single metal cation in one lattice binding site will adopt a distribution of coordination geometries caused by thermally induced structural changes in M–O<sub>f</sub> bonds and (alumino)siloxane rings as we showed recently for the case of isolated Cu<sup>2+</sup> ions in 6-MR of CHA zeolites.<sup>62</sup> Moreover, such d–d transitions are not unique to Co<sup>2+</sup> at lattice binding sites in crystalline zeolitic frameworks and are also observed for Co<sup>2+</sup> exchanged on amorphous supports (e.g., Co/Al<sub>2</sub>O<sub>3</sub>, Co-doped ZnO, Co/Al<sub>2</sub>O<sub>3</sub> SiO<sub>2</sub>).<sup>63–65</sup> Other experimental efforts to identify proximal Al–Al arrangements in zeolites have used 2-dimensional <sup>27</sup>Al MAS NMR spectroscopy,<sup>15,66</sup> but such data provide nonquantitative information about the number of different Al–Al site ensembles present.

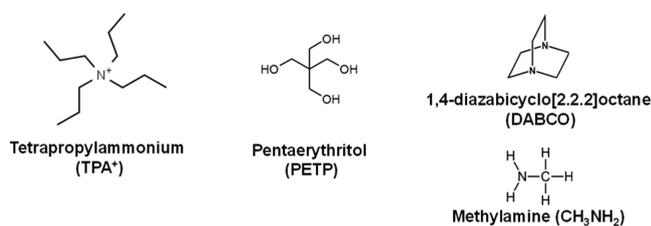
In order to quantitatively assess the number of Al–Al pair arrangements in MFI frameworks, we use here an analogous strategy as in our prior work on CHA frameworks,<sup>52,67</sup> which combines experimental quantification of all available proximal Al sites via Co<sup>2+</sup> titration validated by a cation site balance with theoretical assessments of Co<sup>2+</sup> binding energies at candidate Al–Al pair sites. We then exercise this quantitative characterization tool on a suite of MFI zeolite samples crystallized using tetrapropylammonium (TPA<sup>+</sup>) as the organic SDA in addition to samples crystallized with TPA<sup>+</sup> or with other charge-neutral organic SDAs in combination with higher charge density inorganic SDAs (e.g., Na<sup>+</sup>) to determine their influence on the formation of Al–Al pairs. DFT calculations are used to assess the energetics of TPA<sup>+</sup>–Al<sup>–</sup> interactions to determine a reasonable combinatorial space to consider in efforts to model Al–Al pairs in MFI and to assess Co<sup>2+</sup> exchange energies at these candidate Al–Al pairs. Integration of these experimental

and theoretical assessments provides a foundation to develop quantitative models for Al proximity in the MFI framework, constituting a powerful tool to aid in the development of synthetic strategies to manipulate the formation of proximal sites in MFI zeolites with different catalytic and adsorption properties.

## 2. MATERIALS AND METHODS

**2.1. Synthesis of MFI Zeolites.** Aluminosilicate MFI (ZSM-5) samples were synthesized using various combinations of SDAs (Scheme 1): (i) tetrapropylammonium (TPA<sup>+</sup>) only, (ii) Na<sup>+</sup> and

### Scheme 1. Chemical Structures and Abbreviations for the OSDAs Used To Crystallize MFI in the Presence of Na<sup>+</sup> Cations



TPA<sup>+</sup> as co-SDAs and Na<sup>+</sup> along with the charge-neutral organic SDAs (OSDAs), (iii) pentaerythritol (PETP), or (iv) a mixture of 1,4-diazabicyclo[2.2.2]octane (DABCO) and methylamine (CH<sub>3</sub>NH<sub>2</sub>).

For MFI samples crystallized using TPA<sup>+</sup> as the SDA, procedures were modified from Yokoi et al. using tetrapropylammonium hydroxide (TPAOH) as the TPA<sup>+</sup> source.<sup>46</sup> Synthesis gel molar ratios of 1 SiO<sub>2</sub>/0.003–0.016 Al<sub>2</sub>O<sub>3</sub>/0.611 TPAOH/44 H<sub>2</sub>O were used where the Si/Al ratio in the gel was varied between 30 and 150 at a constant TPAOH/Si ratio of 0.611. The typical synthesis procedure started by preparing a mixture of 3.32 g of TPAOH (Sigma-Aldrich, 40 wt %) and 19.20 g of deionized water (18.2 MΩ) in a perfluoroalkoxy alkane jar (PFA, Savillex Corp.) and stirring for 15 min at ambient conditions. Then 0.20 g of Al(OH)<sub>3</sub> (SPI Pharma, 99%) was added to the synthesis mixture and stirred under ambient conditions for 15 min followed by addition of 3.5 g of amorphous silica (Cabosil M-5, 99%). The solution was then stirred at ambient conditions for 16 h. The solution was then transferred to 45 mL Teflon lined stainless-steel autoclaves (Parr Instruments) and placed in a forced convection oven (Yamato DKN-402C) at 433 K for 5 days. These samples are denoted MFI-TPA(*X*,0) where the *X* is the Si/Al of the solid crystalline material, with the 0 indicating that no Na<sup>+</sup> was present in the synthesis solution.

For MFI samples crystallized using both Na<sup>+</sup> and TPA<sup>+</sup> as co-SDAs, different Na<sup>+</sup>/TPA<sup>+</sup> ratios were used in synthesis gels with molar ratios of 1 SiO<sub>2</sub>/0.01 Al<sub>2</sub>O<sub>3</sub>/0.10–0.611 TPAOH/0–0.26 Na<sub>2</sub>O/44 H<sub>2</sub>O/0.611 OH. The typical synthesis procedure started by preparing a mixture of 3.32 g of TPAOH (Sigma-Aldrich, 40 wt %) and 19.20 g of deionized water in a PFA jar and stirring for 15 min at ambient conditions. Then 0.20 g of Al(OH)<sub>3</sub> (SPI Pharma, 99%) were added to the synthesis mixture and stirred under ambient conditions for 15 min followed by addition of 5.25 g of a 5 M sodium hydroxide (NaOH) solution (16.3 wt %) and 3.5 g of amorphous silica (Cabosil M-5, 99%). The solution was then stirred at ambient conditions for 16 h. The solution was then transferred to 45 mL Teflon lined stainless-steel autoclaves and placed in the forced convection oven at 433 K for 5 days. Samples are denoted MFI-TPA(*X*,*Y*) where *X* is the Si/Al of the solid crystalline material and *Y* is the Na<sup>+</sup>/TPA<sup>+</sup> ratio in the synthesis solution.

For MFI samples crystallized with PETP as the OSDA, a synthesis recipe was adapted from Park et al.<sup>68</sup> with gel molar ratios of 1 SiO<sub>2</sub>/0.01 Al<sub>2</sub>O<sub>3</sub>/0.15 PETP/0.04 Na<sub>2</sub>O/30 H<sub>2</sub>O with 5 wt % of MFI seeds. First, 1.03 g of PETP (Sigma-Aldrich, 99%) was added to 25.56

g of water and stirred for 15 min. Then 0.08 g of Al(OH)<sub>3</sub> (SPI, 99%), 0.15 g of MFI seeds (Zeolyst, CBV5524G), and 1.50 g of NaOH solution (16.3 wt %) were added to the solution, and the mixture was stirred for 15 min. Amorphous silica (Cabosil M-5, 99%) was then added. The solution was aged at 353 K for 18 h before loading into a 45 mL Teflon liner and stainless-steel autoclave for crystallization under static conditions at 453 K for 2 days. This sample is denoted MFI-PETP(43, 0.5) to indicate the solid Si/Al ratio 43 and the synthesis gel Na<sup>+</sup>/PETP ratio.

MFI samples were also crystallized with a mixture of Na<sup>+</sup>, DABCO, and CH<sub>3</sub>NH<sub>2</sub> by adapting a procedure reported in a study of beta zeolite crystallization.<sup>69,70</sup> The synthesis gel molar ratios were 1 SiO<sub>2</sub>/0.0125 Al<sub>2</sub>O<sub>3</sub>/0.36 DABCO/0.36 CH<sub>3</sub>NH<sub>2</sub>/0.014 Na<sub>2</sub>O/13.2 H<sub>2</sub>O. In a typical synthesis, 3.06 g of DABCO (Sigma-Aldrich, 99%) was added to a solution of 8.84 g of deionized water (18.2 MΩ) and 2.09 g of CH<sub>3</sub>NH<sub>2</sub> (Sigma-Aldrich, 40 wt % in water), which was stirred for 30 min. Then 0.09 g of NaOH (Macron, 98%), 0.39 g of aluminum isopropoxide (Sigma-Aldrich, 98%), and 15 g of colloidal silica (Ludox HS-30, Sigma-Aldrich, 30 wt % in water) were added. The solution was stirred at ambient conditions for 4 h and then loaded into a 45 mL Teflon liner and stainless-steel autoclave, which was placed in a static oven at 413 K for 16 days. Samples are denoted MFI-DABCO(*X*,*Y*)-*Z* where *X* is the solid Si/Al ratio, *Y* is the Na<sup>+</sup>/DABCO ratio in the synthesis gel, and *Z* is either 1 or 2 to denote a replicate synthesis.

In all cases, after zeolite crystallization was quenched, solids were washed in deionized water and acetone alternating until the pH was constant between washes. Solids were recovered via centrifugation and then dried at 373 K for 24 h under stagnant air. The dried solids recovered from crystallization experiment procedures were then treated in flowing air at 853 K for 10 h (1.67 cm<sup>3</sup> g<sub>cat</sub><sup>-1</sup>, 0.0167 K s<sup>-1</sup>, 99.999% UHP, Indiana Oxygen) to remove organic content.

**2.2. Preparation of Cation-Exchanged Zeolites.** All samples were subjected to liquid-phase ion exchange with ammonium nitrate in order to remove any residual Na<sup>+</sup>. NH<sub>4</sub><sup>+</sup> ion exchange occurred with a 1 M NH<sub>4</sub>NO<sub>3</sub> solution (solid NH<sub>4</sub>NO<sub>3</sub> ≥ 98%, Sigma-Aldrich) using 150 cm<sup>3</sup> of solution per gram of zeolite while stirring at ambient conditions for 24 h. Afterward, solids were washed four times with deionized water and then dried at 373 K for 24 h. H-form zeolites were obtained by treating dried NH<sub>4</sub>-form zeolites in flowing air to 773 K for 4 h (1.67 cm<sup>3</sup> g<sub>cat</sub><sup>-1</sup>, 0.0167 K s<sup>-1</sup>, 99.999% UHP, Indiana Oxygen). Na-form zeolites were obtained by liquid-phase ion exchange at ambient conditions with a 1 M NaCl solution (5.8 wt % in deionized water, 99.9 wt %, Sigma-Aldrich) using 150 cm<sup>3</sup> of solution per gram of zeolite while stirring at ambient conditions for 24 h. Afterward, solids were washed four times with deionized water, and then dried at 373 K for 24 h. Na-form samples were then treated in flowing air to 773 K for 4 h (1.67 cm<sup>3</sup> g<sub>cat</sub><sup>-1</sup>, 0.0167 K s<sup>-1</sup>, 99.999% UHP, Indiana Oxygen). Na-form samples were converted into partially Co<sup>2+</sup>-exchanged forms by liquid-phase ion exchange using a 0.5 M Co(NO<sub>3</sub>)<sub>2</sub> solution (9.1 wt % cobalt nitrate hexahydrate in deionized water, 99 wt % Sigma-Aldrich) using 150 cm<sup>3</sup> of solution per gram of zeolite at 353 K for 24 h. Co-form zeolites were then washed four times with deionized water, dried at 373 K, and treated in flowing air to 773 K for 4 h (1.67 cm<sup>3</sup> g<sub>cat</sub><sup>-1</sup>, 0.0167 K s<sup>-1</sup>, 99.999% UHP, Indiana Oxygen).

**2.3. Zeolite Characterization.** The framework structures were determined by powder X-ray diffraction (XRD) measured on a Rigaku SmartLab X-ray diffractometer operated at 1.76 kW with a Cu Kα radiation source (λ = 0.154 nm). Approximately 0.01–0.03 g of dried sample was loaded into a zero-background, low-dead-volume sample holder (Rigaku), and the diffraction pattern was measured from 4° to 40° 2θ at a rate of 0.0167° s<sup>-1</sup>.

Micropore volumes were determined from N<sub>2</sub> adsorption isotherms measured on H-MFI samples held at 77 K using Micromeritics ASAP 2020. Approximately 0.02–0.05 g of zeolite samples was pressed and sieved to a uniform size (180–250 μm), degassed by heating under vacuum (<5 mmHg) to 393 K (0.167 K s<sup>-1</sup>) for 2 h, heated, and held at 623 K (0.167 K s<sup>-1</sup>) for 9 h. The uptake of liquid N<sub>2</sub> at 0.05–0.35

$P/P_0$  was extrapolated to zero pressure to estimate micropore volumes.

$^{27}\text{Al}$  magic angle spinning nuclear magnetic resonance (MAS NMR) spectra were measured on the H-MFI samples, which were hydrated for a minimum of 24 h in a desiccator containing saturated potassium chloride.  $^{27}\text{Al}$  NMR spectra were collected using a Chemagnetics CMX-Infinity 400 spectrometer in a wide-bore 9.4 T magnet (Purdue Interdepartmental NMR Facility), were acquired at ambient conditions using a 2.3  $\mu\text{s}$  pulse, an acquisition time of 12.8 ms, and a relaxation delay of 1 s, and were measured at 104.24 MHz and a MAS rate of 5 kHz.

Elemental analysis to measure Na, Al, and Co content was performed using atomic absorbance spectroscopy on a PerkinElmer Model AAnalyst 300 spectrometer. Samples were prepared by digesting 0.01–0.02 g of zeolite powder in 2.5 g of a 48 wt % hydrofluoric acid solution for at least 24 h followed by dilution in approximately 50 g of deionized water [Note: Researchers should use caution when working with HF and should use appropriate personal protective equipment, ventilation, and other safety measures]. Absorbance values for Al, Na, and Co were measured at 309.3 nm in a reducing acetylene nitrous oxide flame and 589.0 and 240.7 nm in an oxidizing acetylene/air flame. Calibrations and known standards were used to determine element concentrations for each sample. Si contents were not measured by AAS; the Si/Al ratio for each sample was calculated from the measured Al content and the unit cell formula.

Thermogravimetric analysis (TGA) on a TA Instruments SDT Q600 thermogravimetric analyzer and differential scanning calorimeter (TGA-DSC) was used to measure organic weight loss on the as-made zeolite solids. Typically, 0.01–0.02 g of the as-made sample was heated in flowing dry air (83.3  $\text{cm}^3 \text{s}^{-1}$ , UHP, 99.999%, Indiana Oxygen) to 523 K (0.167  $\text{K s}^{-1}$ ) and held for 0.5 h to remove adsorbed water before additional heating to 1073 K (0.167  $\text{K s}^{-1}$ ) to combust the occluded organic content. The weight loss during the second temperature ramp (523–1073 K) was taken to be the organic content (details in section S.5, SI).

Diffuse reflectance UV–vis (DRUV–vis) spectra of Co-form MFI samples were collected on a Varian Cary 5000 UV–vis–NIR Spectrophotometer attached with a Harrick Scientific Praying Mantis diffuse reflectance accessory. Baseline spectra were collected at ambient conditions using poly(tetrafluoroethylene) (PTFE, 1  $\mu\text{m}$  powder, Sigma-Aldrich) as the 100% reflectance standard. DRUV–vis spectra were converted to quasi-absorption spectra using the Kubelka–Munk (F(R)) function. Spectra were collected from 12 500 to 50 000  $\text{cm}^{-1}$  at a scan rate of 167  $\text{cm}^{-1} \text{s}^{-1}$  under flowing air (0.833  $\text{cm}^3 \text{s}^{-1}$ , UHP, 99.999%, Indiana Oxygen) at 673 K.

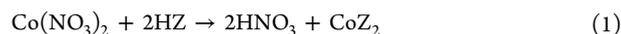
Ammonia temperature-programmed desorption ( $\text{NH}_3$  TPD) was used to quantify the number of  $\text{H}^+$  sites on H-form and Co-form MFI samples, according to procedures described elsewhere, with a Micromeritics AutoChem II 2920 Chemisoption analyzer and a Agilent 5973N mass-selective detector (MSD) system.<sup>71,72</sup> In brief, 0.03–0.06 g of  $\text{NH}_4$ -form and Co-form MFI samples were pelleted and sieved to retain a particle size between 180 and 250  $\mu\text{m}$  and then supported between two quartz wool plugs in a quartz reactor. To quantify total  $\text{H}^+$  sites on  $\text{NH}_4$ -form MFI, samples were held at 323 K for 0.5 h under flowing He (15  $\text{cm}^3 \text{s}^{-1}$  ( $\text{g solid}^{-1}$ ), UHP, 99.999%, Indiana Oxygen) followed by increasing the temperature to 873 K (0.167  $\text{K s}^{-1}$ ) while the effluent gas was sent to the MSD system for analysis. To quantify residual  $\text{H}^+$  sites on Co-form MFI, samples were treated in an oxidative environment (dry air at 0.833  $\text{cm}^3 \text{s}^{-1}$ , UHP, 99.999%, Indiana Oxygen, to 673 K for 2 h, 0.167  $\text{K s}^{-1}$ ), after which  $\text{NH}_3$  titration of  $\text{H}^+$  sites was performed using a gas-phase titration method in which samples were first exposed to flowing  $\text{NH}_3$  (20  $\text{cm}^3 \text{s}^{-1} \text{g}^{-1}$ , 500 ppm of  $\text{NH}_3$  in balance He, Matheson) at 433 K for 4 h and then to a flowing wet He stream ( $\sim 3\%$   $\text{H}_2\text{O}$ , 20  $\text{cm}^3 \text{s}^{-1} \text{g}^{-1}$ ) at 433 K for 8 h in order to desorb  $\text{NH}_3$  bound at nonprotonic sites. Argon pulses of known molar quantities were used to determine a response factor ( $\text{NH}_3/\text{Ar}$ ), and an Ar pulse introduced after each  $\text{NH}_3$  TPD experiment was used to quantify the amount of  $\text{NH}_3$  evolved during the experiment.

**2.4. Computational Methods.** Periodic density functional theory (DFT) calculations were performed with the Vienna ab initio simulation package (VASP)<sup>73–76</sup> using the computational catalysis interface (CCI).<sup>77</sup> Planewaves were constructed with an energy cutoff of 400 eV using the projector augmented wave (PAW) method.<sup>78,79</sup> The Brillouin zone was sampled only at the  $\Gamma$ -point. All calculations were performed using the Perdew–Burke–Ernzerhof (PBE) form of the generalized gradient approximation (GGA)<sup>80</sup> in conjunction with Grimme's DFT-D3 correction with Becke–Johnson damping (D3BJ)<sup>81,82</sup> to account for dispersive forces.

A two-step procedure was used for all optimization calculations to improve computational efficiency.<sup>77</sup> In the first step, wave functions were converged such that they varied by  $<10^{-4}$  eV and structures relaxed until the forces on any atom were  $<0.05 \text{ eV } \text{\AA}^{-1}$ . Forces were computed using a fast Fourier transform (FFT) grid equal to 1.5 $\times$  the planewave cutoff. These settings do not yield accurate forces near minima on potential energy surfaces; thus, structures were further optimized in the second step until wave functions varied  $<10^{-6}$  eV and forces on any atom were  $<0.05 \text{ eV } \text{\AA}^{-1}$  but with a FFT grid 2 $\times$  the planewave cutoff. Calculations for Co-form zeolites were completed with spin polarization. Calculations with charge (e.g., an anionic zeolite framework) included a universal compensating background charge to ensure the net charge for the calculation is zero. Some calculations were performed with the VASPsol<sup>83</sup> implicit solvation model, as described below; unless otherwise noted, these calculations were performed with the relative permittivity of liquid water at 298 K ( $\epsilon = 80$ ).<sup>84</sup>

The MFI structure model was constructed from previous X-ray diffraction (XRD) results with unit cell parameters  $a = 20.078 \text{ \AA}$ ,  $b = 19.894 \text{ \AA}$ ,  $c = 13.372 \text{ \AA}$ , and  $\alpha = \beta = \gamma = 90.0^\circ$  (*Phma* space group).<sup>85</sup> This model has proven sufficiently stable for DFT calculations with guest species and after simulated annealing compared to other common MFI structures used in theoretical investigations.<sup>86</sup> XRD analysis of TPA-loaded MFI crystals identified 24 symmetrically unique T-sites,<sup>87</sup> but we focus on the unique positions Al can occupy upon removal of TPA<sup>+</sup> from the MFI pores; hence, we consider MFI to have 12 symmetrically unique T-sites. The CHA structure model ( $a = b = 13.675 \text{ \AA}$ ,  $c = 14.767 \text{ \AA}$ ,  $\alpha = \beta = 90.0^\circ$ ,  $\gamma = 120.0^\circ$ ) was obtained from the IZA database.<sup>1</sup> CHA is comprised of adjacent 8-, 6-, and 4-MR and has large cage voids typical of small-pore zeolites. CHA has only one symmetrically unique T-site.

$\text{Co}^{2+}$  exchange energies ( $\Delta E_{\text{Co-exch}}$ ) were calculated to determine the Al–Al site pairs that can be titrated using established methods for determining the fraction of sites in proximal arrangements.<sup>50,52,58,67</sup> A  $\text{Co}(\text{NO}_3)_2$  titrant is used, and  $\text{Co}^{2+}$  replaces two protons if the Al are in an appropriate arrangement to accommodate the  $\text{Co}^{2+}$  cation



where  $\text{CoZ}_2$  represents a  $\text{Co}^{2+}$ -exchanged zeolite and 2HZ represents a proton-form zeolite with two Brønsted acid sites. Critically, a proton on an Al<sup>+</sup> can bind to any of the four O atoms adjacent to the Al. In the presence of a proton-shuttling species (e.g.,  $\text{CH}_3\text{OH}$ ), this  $\text{H}^+$  position is equilibrated between these O atoms, as shown by DFT calculations<sup>88–90</sup> and IR spectra of adsorbed pyridine<sup>91</sup> on zeolites; as such, we use a Boltzmann average to represent the energy of these H-form Brønsted acid site pairs

$$\langle E[\text{HZ}] \rangle = \frac{\sum_i E_i e^{-E_i/kT}}{\sum_i e^{-E_i/kT}} \quad (2)$$

where  $E_i$  is the energy of configuration  $i$ , as in previous work.<sup>7,12</sup> We calculate  $\Delta E_{\text{Co-exch}}$  relative to the energies of gas-phase  $\text{Co}(\text{NO}_3)_2$  and  $\text{HNO}_3$  and the ensemble average protonated form of the zeolite

$$\Delta E_{\text{Co-exch}} = 2E[\text{HNO}_3(\text{g})] + E[\text{CoZ}_2] - E[\text{Co}(\text{NO}_3)_2(\text{g})] - \langle E[(\text{HZ})_2] \rangle \quad (3)$$

In this case,  $\langle E[(\text{HZ})_2] \rangle$  represents the ensemble average energy at 353 K of all 16 possible configurations of the two protons on the Brønsted acid site pair. Ewald summations<sup>92</sup> describe the Coulombic

**Table 1. Structural and Site Characterization of MFI Samples Sourced Commercially and Synthesized in This Study**

sample <sup>a</sup>	micropore volume (cm <sup>3</sup> g <sup>-1</sup> ) <sup>b</sup>	Si/Al <sup>c</sup>	Al per unit cell <sup>c</sup>	Al <sub>f</sub> /Al <sub>tot</sub> <sup>d</sup>	H <sup>+</sup> /Al <sub>tot</sub> <sup>e</sup>	H <sup>+</sup> /Al <sub>f</sub> <sup>d</sup>	Co <sup>2+</sup> /Al <sub>tot</sub> <sup>f</sup>	fraction of Al in pairs <sup>g</sup>
MFI(13,C)	0.14	13.2	6.74		0.85		0.17	0.34
MFI(17,C)	0.15	17.3	5.25		0.66		0.21	0.42
MFI(31,C)		30.6	2.81		0.92		0.29	0.58
MFI(43,C)	0.14	43.0	2.56		0.85		0.04	0.08
MFI-TPA(37,0)		37.1	2.52		0.60		0.17	0.34
MFI-TPA(50,0)	0.15	49.8	1.89	0.93	1.01	1.09	0.12	0.24
MFI-TPA(71,0)	0.12	70.9	1.34		1.05		0.06	0.12
MFI-TPA(118,0)	0.13	117.7	0.81	0.86	0.95	1.10	0.01	0.02
MFI-TPA(159,0)	0.16	159.2	0.60	0.87	0.94	1.08	0.04	0.08
MFI-TPA(185,0)	0.14	184.9	0.52	0.92	0.89	0.97	0.01	0.02
MFI-TPA(52,0.25)	0.13	51.6	1.86		1.09		0.06	0.12
MFI-TPA(57,0.75)	0.15	56.7	1.69	0.96	1.10	1.15	0.11	0.22
MFI-TPA(51,1.5)	0.15	50.8	1.89	0.94	0.82	0.87	0.12	0.24
MFI-TPA(58,3)	0.13	57.5	1.67	0.97	1.13	1.16	0.22	0.44
MFI-TPA(55,5)	0.13	54.5	1.76	0.95	0.97	1.02	0.22	0.44
MFI-PETP(43,0.5)	0.11	43.1	2.14	0.92	1.01	1.10	0.03	0.06
MFI-DABCO(44,0.04)-1	0.13	44.1	2.08	0.89	0.87	0.98	0.03	0.06
MFI-DABCO(44,0.04)-2	0.13	44.2	2.07		0.95		0.07	0.14

<sup>a</sup>Sample nomenclature is MFI-OSDA(X,Y), where X is the Si/Al ratio of the solid determined by AAS and Y is the Na<sup>+</sup>/OSDA ratio used in the synthesis solution or 'C' for samples of commercial origin (Zeolyst CBV 2314, 3024E, 5524G, and 8014 in order of increasing Si/Al). For the DABCO samples, the "-1" or "-2" suffix denotes a replicate synthesis. <sup>b</sup>Micropore volumes determined from N<sub>2</sub> adsorption isotherms at 77 K (section S.2, SI). <sup>c</sup>Si/Al ratios and number of Al per unit cell (96 T-site) determined on H-zeolites using AAS (example calculation in section S.6, SI). <sup>d</sup>Determined by <sup>27</sup>Al MAS NMR (section S.3, SI). Uncertainties are ±10%. <sup>e</sup>Determined with liquid-phase NH<sub>4</sub><sup>+</sup> ion exchange followed by TPD (section S.4, SI). Uncertainties are ±0.05. <sup>f</sup>Quantification of proximal Al sites by Co<sup>2+</sup> titration using methods described in sections 3.2.1 and S7. <sup>g</sup>Fraction of Al in pairs, calculated by 2\*Co<sup>2+</sup>/Al<sub>tot</sub>.

interactions in periodic unit cells and were calculated based on a previously reported process<sup>93,94</sup> with a weight parameter ( $\omega = 10$ ) and a numerical accuracy ( $A$  specified as  $10^{-4}$ ) for N and Al interactions with charges of +1 and -1, respectively.

### 3. RESULTS AND DISCUSSION

Table 1 summarizes the site and structural properties of the MFI zeolites synthesized in this work along with four commercially sourced MFI samples (Zeolyst) that have been studied in previous literature reports<sup>14,51,55,58,91,95</sup> that were used for comparison. Samples are denoted MFI-X(Y,Z), where X is the OSDA used, Y is the solid Si/Al ratio, and Z is either the Na<sup>+</sup>/OSDA ratio used in the synthesis solution or "C" for samples of commercial origin. XRD patterns (Figures S1–S3, SI) and micropore volumes calculated from N<sub>2</sub> adsorption isotherms (77 K, Figures S5–S7, SI) were characteristic of the MFI framework topology based on comparisons to the IZA database<sup>1</sup> and to samples of commercial origin (Figures S4 and S8, SI). The fraction of total Al (Al<sub>tot</sub>) present as framework Al sites (Al<sub>f</sub>) was estimated from <sup>27</sup>Al MAS NMR spectra of hydrated samples (Figures S9–S11, SI) to make semi-quantitative comparisons of framework Al content among different samples (Table S1, SI); accurate quantification of the Al<sub>f</sub> content from <sup>27</sup>Al MAS NMR spectra is complicated because some tetrahedrally coordinated Al change structure when hydrated forms of zeolites are exposed to other conditions<sup>96–99</sup> and because not all Al species are detected in <sup>27</sup>Al MAS NMR spectra.<sup>91,100</sup> These complications are avoided when using methods to titrate protons directly with a monovalent cation, such as by liquid-phase cation exchange (e.g., Na<sup>+</sup>, NH<sub>4</sub><sup>+</sup>) or by gas-phase adsorption of a probe base (e.g., pyridine, ammonia). Here, protons on H-form MFI samples were quantified using liquid-phase NH<sub>4</sub><sup>+</sup> exchange followed by NH<sub>3</sub> TPD (Figures S12–S14, SI) and are summarized as H<sup>+</sup>/Al<sub>tot</sub> and H<sup>+</sup>/Al<sub>f</sub> values in Table 1. The

number of Brønsted acid sites was similar to the total Al content (H<sup>+</sup>/Al<sub>tot</sub> = 0.85–1.13) on each sample except MFI(17,C), which showed a lower value of 0.66 H<sup>+</sup>/Al<sub>tot</sub> that is consistent with values measured independently in prior work using in situ pyridine (H<sup>+</sup>/Al<sub>tot</sub> = 0.65) and ex situ NH<sub>3</sub> (H<sup>+</sup>/Al<sub>tot</sub> = 0.52) titration.<sup>95</sup>

Section 3.1 examines the influence of tetrapropylammonium (TPA<sup>+</sup>) as the sole SDA to crystallize MFI zeolites, and DFT calculations were performed to assess the stability of Al atoms incorporated at each T-site when compensated by 1 TPA<sup>+</sup> cation and a variety of Al–Al site pair configurations when compensated by two TPA<sup>+</sup> cations. In light of the conflicting methods reported in the literature for selective Co<sup>2+</sup> aqueous ion exchange at proximal Al sites in MFI, we then describe in section 3.2 how integrating results from experiment and theory can be used to develop validated protocols for quantitative Co<sup>2+</sup> titration of certain Al–Al site pairs in MFI. In sections 3.3 and 3.4, we then investigate how Al proximity in MFI is influenced by adding a higher charge-density inorganic cation (Na<sup>+</sup>) to synthesis media that contains either a lower charge-density cationic (TPA<sup>+</sup>) or neutral (pentaerythritol (PETP) or 1,4-diazabicyclo[2.2.2]octane (DABCO)) OSDA, respectively.

**3.1. Influence of TPA<sup>+</sup> on Al Siting in MFI Zeolites.**  
**3.1.1. Evidence for Occlusion of 1 TPA<sup>+</sup> per MFI Channel Intersection.** Crystallization of MFI over a wide range of Al content in the synthesis gel (Si/Al = 30–150) was attempted in the presence of TPA<sup>+</sup> as the sole SDA with other synthesis parameters held constant (OH<sup>-</sup>/Si, water content, precursor compounds, synthesis time, and temperature). Elemental analysis of as-made MFI samples to check for trace Na content, which might have originated from adventitious impurities in the specific reagent or precursor compounds used, showed values below detection limits ( $7 \times 10^{-5}$  mol Na (g<sub>solid</sub>)<sup>-1</sup>), indicating that only TPA<sup>+</sup> guided the crystallization of this suite of MFI samples. TGA of as-made MFI-TPA(X,0)

samples indicated an organic weight loss of 12–13% (Table S2, SI) as also reported previously;<sup>46,101</sup> such values are consistent with the occlusion of 1 TPA<sup>+</sup> cation per MFI channel intersection, as shown in Figure 1 (details in section

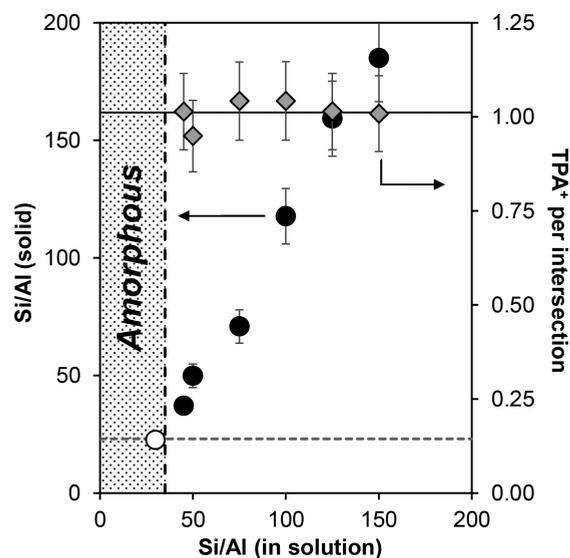


**Figure 1.** Dependence of solid Si/Al ratio (●) and occluded TPA<sup>+</sup> per intersection (◆) in MFI-TPA(X,0) zeolites crystallized using only TPA<sup>+</sup>. Horizontal solid line indicates the average number of TPA<sup>+</sup> per intersection among this series of samples. Shaded gray region (synthesis composition separated by a vertical dashed line, Si/Al = 35) and open circle (○) correspond to formation of amorphous products, and horizontal dashed line represents the predicted CDM limit (Si/Al = 23). Error bars are  $\pm 10\%$ .

S.5, SI). Indeed, earlier studies by Chao et al.<sup>102</sup> and Koningsveld et al.<sup>85</sup> used crystal refinement of X-ray diffraction patterns of MFI to indicate TPA<sup>+</sup> was occluded in their channel intersections, and subsequent studies by Burkett and Davis<sup>103,104</sup> and by Chang and Bell<sup>105</sup> used cross-polarization <sup>1</sup>H–<sup>29</sup>Si MAS NMR, <sup>29</sup>Si NMR, and XRD to provide evidence of organization of silicate clathrates around TPA<sup>+</sup> cations that are precursors to forming MFI channel intersections (Si/TPA<sup>+</sup> = 20–24).<sup>105</sup> Increasing the gel Si/Al ratio led to increases in the solid Si/Al ratio (Figure 1) with crystallization experiments using gel Si/Al ratios > 45 producing crystalline MFI phases with solid Si/Al ratios > 37, which corresponds to <2.5 Al per unit cell (Table 1). In contrast, a gel Si/Al ratio of 30 led to an amorphous product after 7 days at 433 K (Figure 1). Charge density mismatch (CDM) theory proposes that zeolite crystallization requires charge balance between the cationic charges within occluded SDAs and the anionic lattice charges formed by framework Al substitution or by lattice defects;<sup>106–111</sup> as a result, the geometric considerations that determine the upper limit of SDA occupancy of void spaces determine the upper limit of framework Al content. When applied to the MFI framework topology, CDM theory would predict that each TPA<sup>+</sup> cation at full occupancy (4 per 96 T-site unit cell; section S.5, SI) would balance one framework Al (4 Al per unit cell or Si/Al = 23; Figure 1, horizontal dashed line) but that higher framework Al contents are not accessible using TPA<sup>+</sup> alone. This prediction by CDM theory is consistent with the data in Figure 1, as MFI crystallization appears to show a crystallization barrier approaching this theoretical limit under the synthesis conditions studied here

(Figure 1, vertical dashed line at a solid Si/Al = 35). The goal of this study was not to determine the exact composition boundary corresponding to the CDM limit when using TPA<sup>+</sup> as the SDA, as prior studies of MFI crystallization using TPA<sup>+</sup> alone have reported crystallization of MFI with Si/Al = 25<sup>112</sup> and crystallization of MFI with Si/Al < 25 but at much lower temperature (373 K) and with concomitant generation of a large fraction of anionic lattice defects.<sup>113</sup> Further evidence of this CDM barrier and the absence of adventitious Na<sup>+</sup> in the TPA<sup>+</sup>-only synthesis experiments performed here is evident in the successful crystallization of MFI at solid Si/Al ratios < 24 (typically Si/Al  $\approx$  15) when small amounts of NaOH are added to synthesis gels (Si/Al = 25, Na/Si < 0.12, details in section S.6, Figure S17, SI). Studying the crystallization of MFI zeolites with lower Al contents (Si/Al > 185) using only TPA<sup>+</sup> cations was also not a goal of this work but is possible even in the limit of fully siliceous MFI.<sup>103,104</sup> These syntheses, however, often require the addition of other anions (e.g., F<sup>-</sup>) to compensate for TPA<sup>+</sup>, which otherwise would form increasing amounts of anionic lattice defects<sup>114</sup> with decreasing Al content that may eventually inhibit MFI crystallization.

**3.1.2. Energies of Al Substitution with One TPA<sup>+</sup> in the MFI Unit Cell.** We next turn to DFT to assess the energetics associated with Al substitution in MFI lattices when TPA<sup>+</sup> is the sole charge-compensating cation. TPA<sup>+</sup> is expected to occlude within each MFI intersection during synthesis and be charge compensated by either an Al<sup>-</sup> or a siloxy defect (Si–O<sup>-</sup>). To simplify DFT models that examine the interactions between TPA<sup>+</sup> and anionic Al<sup>-</sup> centers, we placed and optimized one TPA<sup>+</sup> cation in the MFI channel intersection with Al substituted at each of the 96 T-site locations in the unit cell. We performed these calculations with and without implicit solvation because zeolites are synthesized in aqueous solution, which could affect the distance between the N center of the TPA<sup>+</sup> and the lattice Al<sup>-</sup> sites and thus the stability of each TPA<sup>+</sup>–Al<sup>-</sup> configuration. A TPA<sup>+</sup> binding energy (with and without solvation) is then calculated to evaluate the relative stabilities as

$$\Delta E_{\text{TPA}} = E[\text{TPA}^+\text{Al}^-] - E[\text{TPA}^+] - E[\text{Al}^-] \quad (4)$$

where  $E[\text{TPA}^+\text{Al}^-]$  is the energy of the TPA-form structure,  $E[\text{Al}^-]$  is the energy of the anionic zeolite, and  $E[\text{TPA}^+]$  is the energy of gas-phase TPA<sup>+</sup> cation. TPA<sup>+</sup> binding energies (Figure 2a) indicate a preference for Al substitution near the N

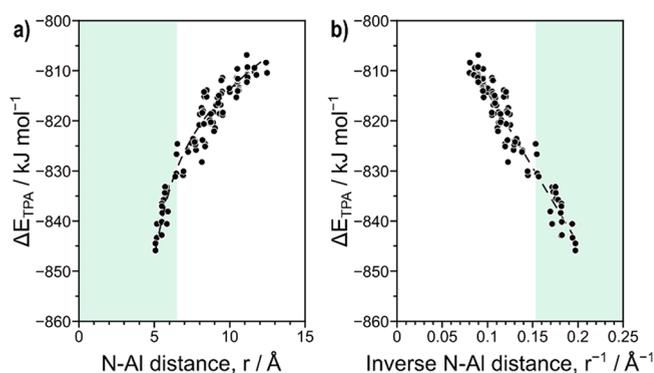


**Figure 2.** TPA<sup>+</sup> binding energies ( $\Delta E_{\text{TPA}}$ , eq 4) as a function of (a) the distance between the N of the TPA<sup>+</sup> and the Al of the framework and (b) the inverse of this distance. Shaded green region indicates a < 6.5 Å cutoff distance; dashed lines are provided to guide the eye.

**Table 2. Relative Al Exchange Energies ( $\Delta E_{\text{TPA-Al}}$ ),  $\text{TPA}^+$  Binding Energies ( $\Delta E_{\text{TPA}}$ , eq 4),  $\text{N}^+-\text{Al}^-$  Distances of TPA-Form MFI, and Relative Al<sup>-</sup> Energies ( $\Delta E_{\text{Al}^-}$ ) at All 12 T Sites for the Most Stable Position of Substitution for Each Unique T-Site<sup>a</sup>**

T-site	void environment <sup>b</sup>			$\Delta E_{\text{Al}^-}$ (kJ mol <sup>-1</sup> )		$r_{\text{N-Al}}$ (Å)		$\Delta E_{\text{TPA-Al}}$ (kJ mol <sup>-1</sup> )		$\Delta E_{\text{TPA}}$ (kJ mol <sup>-1</sup> )	
	int.	str.	sin.	vacuum	$\epsilon = 80$	vacuum	$\epsilon = 80$	vacuum	$\epsilon = 80$	vacuum	$\epsilon = 80$
T1	X	X	X	12	12	5.15	5.15	15	16	-843	-722
T2	X	X	X	5	5	5.62	5.68	15	13	-836	-718
T3	X	X	X	7	3	5.49	5.49	12	11	-840	-719
T4			X	5	8	7.24	8.36	25	18	-826	-716
T5	X	X		15	12	5.50	7.76	24	22	-837	-716
T6	X	X	X	22	17	5.79	7.71	33	28	-834	-716
T7	X	X		13	16	6.39	6.38	27	23	-831	-719
T8	X	X		4	7	8.15	8.14	21	14	-828	-719
T9	X	X	X	14	12	5.70	6.94	25	19	-834	-719
T10	X		X	15	17	5.52	5.52	18	18	-843	-725
T11	X	X		6	9	5.83	5.83	12	10	-841	-725
T12	X	X	X	0	0	5.07	5.07	0	0	-846	-726

<sup>a</sup>Effects of the aqueous solvent were examined using VASPsol with a relative permittivity ( $\epsilon$ ) of 80. <sup>b</sup>Intersection (int.), straight channel (str.), and sinusoidal channel (sin.) void environments are denoted here for each T-site based on the locations of the accessible O atoms around that site and their ability to catalyze reactions in those environments.

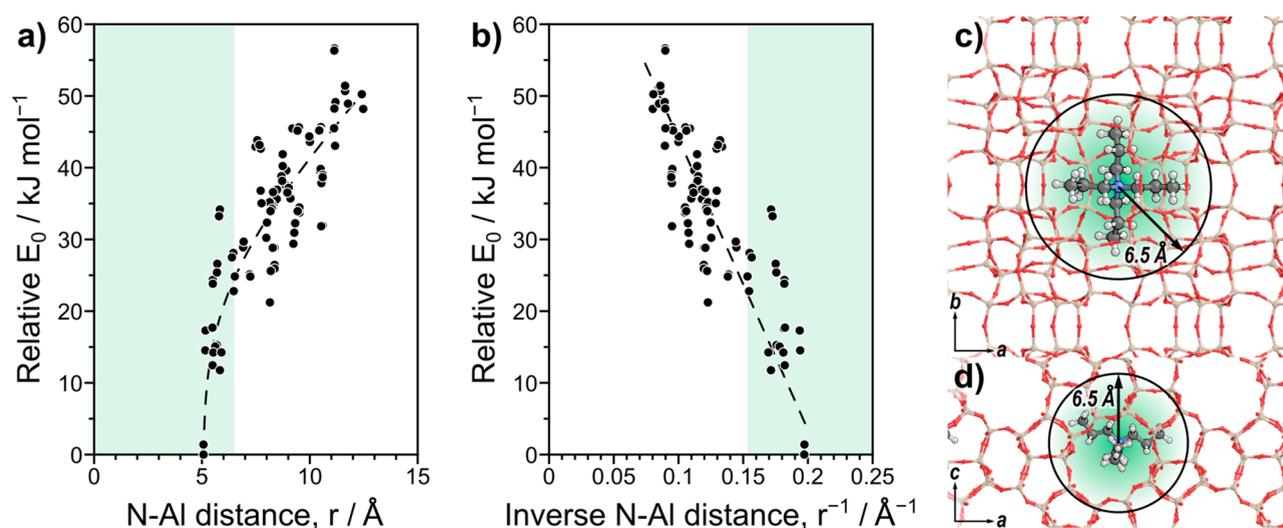


**Figure 3.** Relative energy of MFI with one  $\text{TPA}^+$  and one Al in the unit cell ( $\Delta E_{\text{TPA-Al}}$ ), where Al is substituted at each of the 96 T-site locations as a function of (a) the distance between the N of the  $\text{TPA}^+$  and the Al of the framework and (b) the inverse of this distance. Green boxes indicate a 6.5 Å cutoff distance, and dashed lines are to guide the eye.  $\text{TPA}^+$  in the intersection of Si-form MFI with the 6.5 Å radial cutoff shown with a black circle down (c) the  $c$  vector and (d) the  $b$  vector of the unit cell.

centers of  $\text{TPA}^+$ , evident in the  $\Delta E_{\text{TPA}}$  values that increase from a minimum of  $-846 \text{ kJ mol}^{-1}$  at a  $\text{N}^+-\text{Al}^-$  distance ( $r_{\text{N-Al}}$ , the distance between the nuclei of the N and Al atoms) of 5.07 Å to values less negative than  $-828 \text{ kJ mol}^{-1}$  above 7 Å. These  $\Delta E_{\text{TPA}}$  values are very exothermic because of the unphysical gas-phase  $\text{TPA}^+$  cation reference state, but their relative values can be compared to determine the relative energetics of various  $\text{TPA}^+-\text{Al}^-$  configurations. These  $\Delta E_{\text{TPA}}$  values linearly decrease and become more exothermic with inverse  $\text{N}^+-\text{Al}^-$  distance (Figure 2b), indicating that a Coulombic interaction governs the interaction energies between  $\text{TPA}^+$  and  $\text{Al}^-$

$$\Delta E_{\text{TPA}} \propto \frac{q_i q_j}{r_{ij}} \quad (5)$$

where  $q_i$  and  $q_j$  represent the charges (taken here as +1 for  $\text{TPA}^+$  and -1 for  $\text{Al}^-$ ) and  $r_{ij}$  is given as  $r_{\text{N-Al}}$ . Furthermore, this strong trend of  $\Delta E_{\text{TPA}}$  with  $\text{N}^+-\text{Al}^-$  distance indicates that

anionic charge can be approximated as a point charge at the location of the framework Al in this Coulombic interaction. As such, Al substitution preferentially occurs at lattice positions located near the N center of  $\text{TPA}^+$ . This  $\text{TPA}^+$  binding energy, however, does not account for the influence of intrinsic Al-siting preferences in the MFI lattice that arise from differences in the local environment of each of the 12 distinct T-sites (e.g., preferred bond angles, framework density).

Intrinsic Al-siting preferences were calculated by comparing the anionic forms of the framework (without a charge-compensating cation) containing Al substituted at each of the 12 T-sites in MFI ( $\Delta E_{\text{Al}^-}$ , Table 2); such values are unadulterated by the interaction of  $\text{Al}^-$  with a cationic SDA or a proton and how such cations would interact with their local environment. Without any cations, Al prefers to substitute at T12, which is 4  $\text{kJ mol}^{-1}$  more stable than the second-best location (T8) and 22  $\text{kJ mol}^{-1}$  more stable than the worst location (T6). Most Al T-site locations are bonded to O atoms that are accessible to intersection or channel voids

(Table 2), and there is no systematic trend in  $\Delta E_{\text{Al-}}$  with T-site position that would indicate any preference for Al siting in locations that bias toward any specific void environment (Table 2).

Prior DFT calculations indicated that the stabilities of H-form MFI vary by up to 37 kJ mol<sup>-1</sup> and that Al was most stable when substituted at T7 and least stable at T9.<sup>115</sup> Additional investigations using Hartree–Fock<sup>116</sup> and semi-empirical methods<sup>117</sup> on small clusters derived from MFI (5T and 8T, respectively) found that the H-form was most stable with Al at the T12 position. These previous studies, however, compared relative Al locations with a proton, the stability of which can be affected by the environment around each T-site and therefore do not reflect intrinsic Al-siting preferences or the preferences of Al location during crystallization when other cationic species (such as TPA<sup>+</sup>) can balance lattice charges. Other calculations on 1T clusters derived from MFI without a charge-compensating proton using Hartree–Fock found that Al's located at T6, T9, and T12 were most stable;<sup>118</sup> however, these (and other small cluster investigations<sup>116,117</sup>) do not capture effects of the long-range structure of MFI.

Relative Al exchange energies ( $\Delta E_{\text{TPA-Al}}$ ) accounting for TPA<sup>+</sup> being present in the MFI intersection were calculated to determine the most stable Al location for each of the 12 T-sites (Table 2, structures shown in Figures S24, SI). The most stable position of Al is at the nearest T12 position, both with and without implicit solvation, as the T12 site places Al closest to the N center in TPA<sup>+</sup> after optimization ( $r_{\text{N-Al}} = 5.07$  Å without solvation); however, this low energy also reflects an intrinsic preference for Al substitution at this position as indicated by its  $\Delta E_{\text{Al-}}$  value.

Configurations with Al at all other T-sites are at least 10 kJ mol<sup>-1</sup> less stable than T12 despite many placing Al similarly close to the N center in TPA<sup>+</sup>. For example, the most favorable T1 location places Al 5.15 Å from the N center in TPA<sup>+</sup> (second closest location) but is 16 kJ mol<sup>-1</sup> higher in energy than Al at T12 because Al is intrinsically 12 kJ mol<sup>-1</sup> less stable at T1 than at T12 ( $\Delta E_{\text{Al-}}$ , Table 2). Thus, the relative Al exchange energies ( $\Delta E_{\text{TPA-Al}}$ ) are dictated by a combination of intrinsic Al site preferences and interaction energies between TPA<sup>+</sup> and Al<sup>-</sup> ( $\Delta E_{\text{TPA}}$ ) as shown by the increase in scatter when comparing the correlations of  $\Delta E_{\text{TPA}}$  and  $\Delta E_{\text{TPA-Al}}$  with  $r_{\text{N-Al}}$  (Figures 2 and 3), where the latter does not account for intrinsic Al energies. A simple correlation to predict the relative Al exchange energy is given by

$$\Delta E_{\text{TPA-Al}} = \alpha k_e \frac{q_i q_j}{r_{ij}} + \Delta E_{\text{Al-}} + c \quad (6)$$

where  $k_e$  is Coulomb's constant,  $\alpha$  is a factor that scales the Coulombic interaction, and  $c$  is an arbitrary constant for these relative energies. This correlation provides excellent agreement (mean absolute error (MAE) = 2.0 kJ mol<sup>-1</sup>) with calculated values (parity plot in Figure S28a, SI) with residual scatter likely arising from the restructuring of TPA<sup>+</sup> or the framework that may occur for certain TPA–Al arrangements. Coulombic interactions within a periodic model are best handled through Ewald summations, which combine real and reciprocal space interactions to include long-range Coulombic effects.<sup>92</sup> Here, a correlation based on Ewald summations is also computed

$$\Delta E_{\text{TPA-Al}} = \beta E_{\text{Ewald}} + \Delta E_{\text{Al-}} + c \quad (7)$$

where  $\beta$  scales the Ewald summation term and gives a MAE of 1.8 kJ mol<sup>-1</sup> (parity plot in Figure S28b, SI).

Previous work examining interactions between the *N,N,N*-trimethyl-1-adamantylammonium (TMAda<sup>+</sup>) SDA and Al<sup>-</sup> sites in the CHA framework showed that implicit solvation models decrease the energy of substituting Al farther from the cationic N center of the SDA.<sup>119</sup> Similar long-range interactions in MFI between framework Al<sup>-</sup> and TPA<sup>+</sup> are attenuated by implicit solvation, such that TPA-form structures with larger N<sup>+</sup>–Al<sup>-</sup> distances have lower relative energies with solvation included (Table 2). The preferences for substitution at each of the unique T-site locations, however, remain largely unchanged; T12 remains the preferred site for Al based on  $\Delta E_{\text{Al-}}$  and the relative energies of Al at T3, T2, T8, T4, and T11 remain <10 kJ mol<sup>-1</sup> (Table 2). These lower relative energies and similar trends indicate that implicit solvation screens electrostatic interactions. As such, the amount that the Coulombic interaction ( $k_e q_i q_j / r_{ij}$  in eq 6 or  $E_{\text{Ewald}}$  in eq 7) governs the relative energies ( $\Delta E_{\text{TPA-Al}}$ ) decreases with solvation included, as demonstrated by decreases in  $\alpha$  and  $\beta$  by factors of ~3 in fitted forms of eqs 6 and 7, respectively (Table 3); the quality of the fits, as represented by the MAE, is

**Table 3. Parameters for Models Used To Predict TPA-Form Energies with One TPA<sup>+</sup> in the MFI Unit Cell Based on a Coulombic Model (eq 6) and Ewald Summations (eq 7)**

	Coulombic model		Ewald summation	
	vacuum	$\epsilon = 80$	vacuum	$\epsilon = 80$
scaling parameter, $\alpha$ or $\beta$	0.22	0.085	0.066	0.027
MAE (kJ mol <sup>-1</sup> )	2.0	1.9	1.8	1.5

largely unaffected by the type of model or the presence or absence of solvation. Thus, we focus on calculations that have been performed without solvation for the remainder of this work, understanding that solvation will typically attenuate energy differences between structures that are calculated in vacuum, and therefore, the energy differences we compute are likely overestimates of the energy differences present in real systems.

Upon examining the energetics of all 96 Al locations, the substitution of Al in locations >6.5 Å from the N center of the TPA<sup>+</sup> results in structures that are >20 kJ mol<sup>-1</sup> less stable without solvent (>14 kJ mol<sup>-1</sup> with solvent) than the most stable TPA–Al configuration (Figure 3a). This indicates that an approximate radial cutoff of 6.5 Å can be applied to identify reasonable locations for siting Al around a TPA<sup>+</sup> cation (Figure 3c and 3d).

**3.1.3. Preferred Al Configurations with Two TPA<sup>+</sup> in the MFI Unit Cell.** Next, we investigate the stability of Al–Al pair configurations, which require two charge-compensating TPA<sup>+</sup> cations to be placed within the four channel interactions of the MFI unit cell. If two TPA<sup>+</sup> are occluded in the MFI unit cell, three unique configurations of TPA<sup>+</sup> are possible (Figure 4), wherein the propyl branches of two adjacent TPA<sup>+</sup> share a straight channel or a sinusoidal channel or do not share a common channel. There are 13 680 possible ways to place two Al in these various two TPA<sup>+</sup> structures (3 × 96 × 95 × 0.5, given by 3 two-TPA<sup>+</sup> configurations, 96 T-sites locations for the first Al, 95 for the second, and 0.5 because these two Al are interchangeable). However, based on the calculations performed with one TPA<sup>+</sup> (section 3.1.2), Al atoms were initially only substituted such that no Al or N centers were



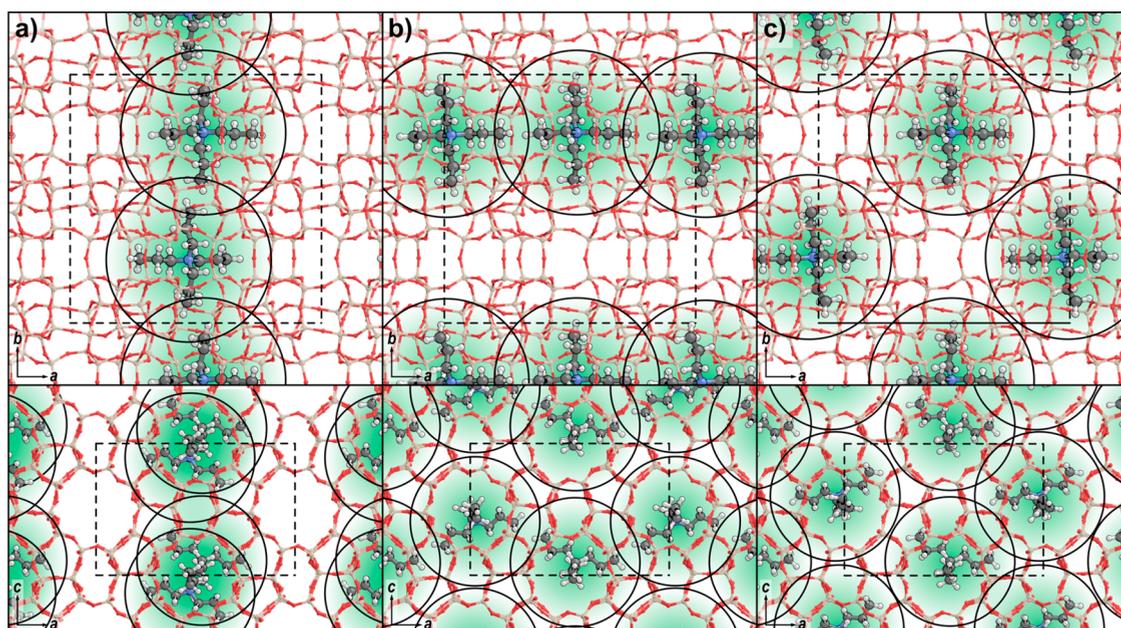


**Figure 4.** Three unique configurations of two TPA<sup>+</sup> in a MFI unit cell: (a) collocation of a propyl branch in the straight channel or (b) sinusoidal channel or (c) no collocation in any channel. All views are shown down the *c* vector (top) and *b* vector (bottom) of MFI, and boundaries of the unit cell are highlighted with a dashed black line. The 6.5 Å cutoff is shown around each TPA<sup>+</sup> with a black circle.

located more than 6.5 Å away from their nearest N or Al counterion; for T4, this distance was extended to 7.5 Å because all N<sup>+</sup>–Al<sup>–</sup> distances are >7 Å for Al substitution at T4 (Table 2). In addition, we included Al–Al pairs in nearest neighbor (NN), next-nearest neighbor (NNN), and next-next-nearest neighbor (NNNN) configurations for the most stable 1-TPA<sup>+</sup> structures identified in Table 2, regardless of N<sup>+</sup>–Al<sup>–</sup> distances, to analyze the stability of proximal Al that do not conform to this distance cutoff. Al–Al pairs in NN configurations are unlikely to form during synthesis because of Löwenstein’s rule but were modeled to examine how Al–Al distances influenced energies. These criteria identify a total of 1773 TPA<sub>2</sub>–Al<sub>2</sub> configurations that were examined out of the 13 680 total possibilities.

The relative Al exchange energies, as discussed in section 3.1.2, predominantly reflect the Coulombic interactions between TPA<sup>+</sup> and Al<sup>–</sup> as well as the intrinsic stabilities of Al at the symmetry-distinct lattice sites. Prior work in CHA has shown that the energy of the framework with two Al decreases (becomes more stable) as the Al–Al distance increases in a manner consistent with a purely Coulombic interaction (i.e., the energy correlates linearly with the inverse of the Al–Al distance).<sup>118</sup> Anion energies in MFI, however, are convoluted by the intrinsic Al-siting preferences among the 12 T-sites, which is a complication absent in CHA because it has a single crystallographic T-site. TPA<sub>2</sub>–Al<sub>2</sub> structures have 6 ionic interactions (4 attractive, 2 repulsive), neglecting long-range periodic interactions. Thus, the relative *E*<sub>0</sub> of a TPA<sub>2</sub>–Al<sub>2</sub> arrangement ( $\Delta E_{\text{TPA}_2-\text{Al}_2}$ ) correlates with the sum of these Coulombic interactions

$$\Delta E_{\text{TPA}_2-\text{Al}_2} \propto \sum_{i,j} k_e \frac{q_i q_j}{r_{ij}} \quad (8)$$

as shown in Figure 5a. Additional variation in the relative TPA-form energy arises from intrinsic Al site preferences as shown

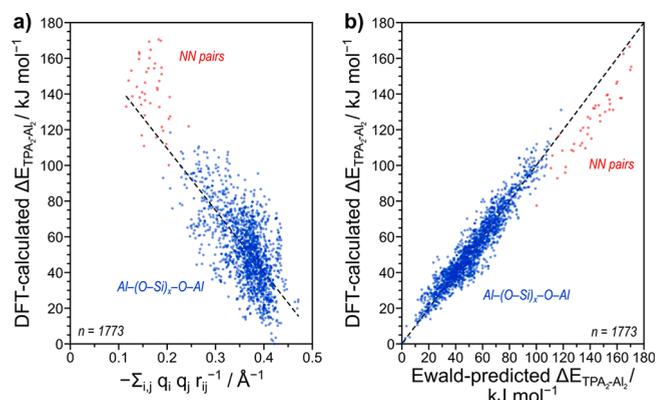


**Figure 5.** DFT-calculated relative TPA-form *E*<sub>0</sub> ( $\Delta E_{\text{TPA}_2-\text{Al}_2}$ ) for configurations at nearest-neighbor (NN) positions that violate Löwenstein’s rule (NN pairs, red, *n* = 42) and those that do not (Al–(O–Si)<sub>*x*</sub>–O–Al, blue, *n* = 1731) as a function of (a) the sum of Coulombic interactions (term contained within eq 9) and (b) the predicted energy from an Ewald summation and intrinsic Al stability (eq 10). Dashed line in a represents a linear fit, while in b the dashed line represents parity.

by adapting the correlation used for the TPA–Al structures (eq 6) to describe these TPA<sub>2</sub>–Al<sub>2</sub> structures

$$\Delta E_{\text{TPA}_2-\text{Al}_2} = \alpha \sum_{i,j} k_e \frac{q_i q_j}{r_{ij}} + \sum_i \Delta E_{\text{Al}_i^-} + c \quad (9)$$

where  $\alpha$  is a scaling constant and  $\Delta E_{\text{Al}_i^-}$  reflects the intrinsic site preference of each Al in the structure (Table 2) in the absence of cations or a second Al (to avoid anion–anion interactions, which are included in the Coulombic expression). This correlation yields a MAE of 6.1 kJ mol<sup>–1</sup>, indicating that the energies of TPA<sub>2</sub>–Al<sub>2</sub> structures are also predominantly governed by Coulombic interactions (Figure S29, SI) and intrinsic Al<sup>–</sup> stabilities. This MAE (6.1 kJ mol<sup>–1</sup>) is slightly

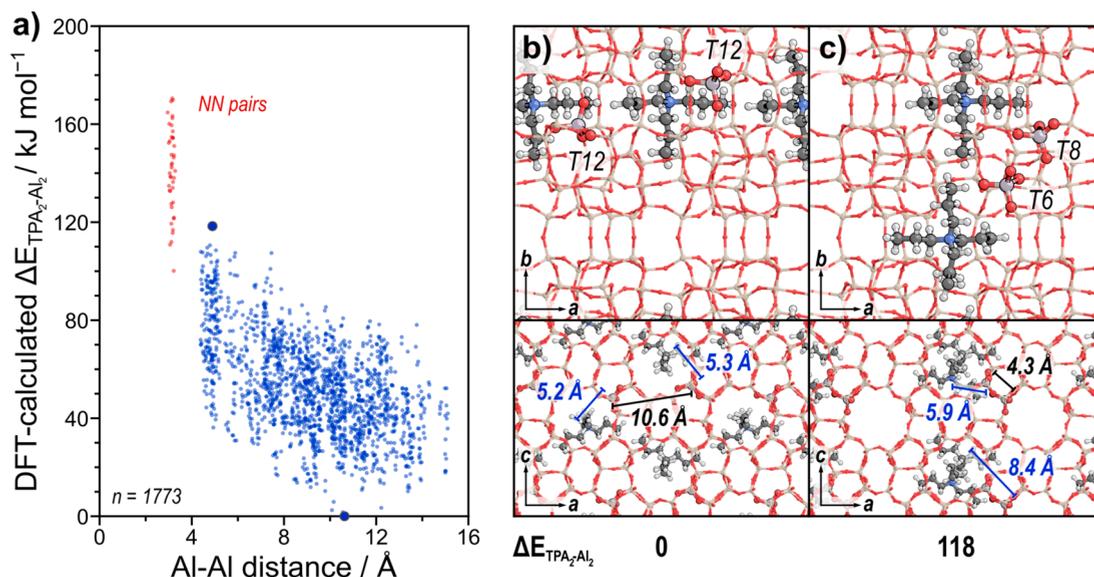


**Figure 6.** (a) Relative TPA-form  $E_0$  ( $\Delta E_{\text{TPA}_2-\text{Al}_2}$ ) for all calculated configurations of two Al atoms in the MFI unit cell in NN configurations (violating Lowenstein's rule, red) and in other (blue) configurations. (b) Most stable TPA-form structure (a T12–T12 pair) and (c) an unstable TPA-form structure (T6–T8 pair) viewed along the  $c$  vector (top) and along the  $b$  vector (bottom) of MFI. Al–Al distances (black) and N–Al distances (blue) for each TPA<sup>+</sup> are shown.

higher than that for the fit of single TPA–Al data (MAE = 2.0 kJ mol<sup>−1</sup>; eq 6), which may reflect the fact that the intrinsic Al<sup>−</sup> term in eq 9 is based on isolated Al<sup>−</sup> calculations and thus would not capture any effects of Al–Al interactions on intrinsic Al<sup>−</sup> stabilities, such as changes in the local geometry of each Al arising from the presence of the other Al in the unit cell. The trends in Al site preferences, however, do not appear significantly affected by the presence of two Al in the MFI unit cell (additional discussion in section S10, SI).

Ewald summations can be applied to TPA<sub>2</sub>–Al<sub>2</sub> to predict relative stabilities similarly to those used to predict energies of 1-TPA<sup>+</sup> structures

$$\Delta E_{\text{TPA}_2-\text{Al}_2} = \beta E_{\text{Ewald}} + \sum_i \Delta E_{\text{Al}_i^-} + c \quad (10)$$

This correlation using Ewald summations is in good agreement with DFT-calculated relative energies of TPA<sub>2</sub>–Al<sub>2</sub> structures (parity plot in Figure S2b) with a MAE of 5.2 kJ mol<sup>−1</sup>, similar to that fit from eq 9. Energies predicted by eqs 9 and 10 (Figure 5) are nearly always underpredicted for NN pairs, suggesting that treating the intrinsic Al<sup>−</sup> terms based on isolated Al data excludes an additional penalty associated with NN pairs.

The relative energies of TPA<sub>2</sub>–Al<sub>2</sub> structures ( $\Delta E_{\text{TPA}_2-\text{Al}_2}$ ) are generally higher when Al–Al distances are smaller because short Al–Al distances result in greater Coulombic repulsion between Al<sup>−</sup> (Figure 6), consistent with prior work.<sup>118</sup> Short Al–Al distances also result in larger Al–N distances, on average, as the TPA<sup>+</sup> are constrained to intersection positions (Figure 3). Configurations with two Al violating Löwenstein's rule are very unstable with  $\Delta E_{\text{TPA}_2-\text{Al}_2} > 100$  kJ mol<sup>−1</sup> for all 42 structures, reflecting strong anion–anion repulsion. Implicit solvation simply reduces the influence of the electrostatic terms in eqs 6 and 7 in determining relative TPA–Al energies but does not significantly change preferences for Al positions, as observed for the single TPA–Al configurations in section 3.1.2. Therefore, while we do not directly compute these

values, we anticipate that solvation would not alter the preference for Al–Al pairs separated by larger distances but could reduce the relative energies of other configurations.

Importantly, Al sites can be close to one another (within ~5 Å) while remaining close to the TPA<sup>+</sup> (within ~7 Å). Some of these arrangements have relatively low  $\Delta E_{\text{TPA}_2-\text{Al}_2}$  near 40 kJ mol<sup>−1</sup>, which should decrease with solvation. This Al–Al distance serves as an important reference point as Al pairs arranged in the 6-MR of CHA are 5.3–6.1 Å apart and have been shown to selectively bind Co<sup>2+</sup> ions.<sup>52,67</sup> Identification of stable configurations that place two Al separated by <5 Å, given that our models were constrained to only two TPA<sup>+</sup> in the unit cell and N<sup>+</sup>–Al<sup>−</sup> distances < 6.5 Å, indicates that such configurations can be stabilized using only TPA<sup>+</sup> as the charge-compensating cation. Next, Co<sup>2+</sup> titration of MFI synthesized with TPA<sup>+</sup> as the sole SDA is used to provide experimental evidence for the formation of these proximal Al–Al configurations suggested by DFT.

**3.2. Influence of TPA<sup>+</sup> on the Formation of Proximal Al Sites in MFI.** 3.2.1. *Experimental Co<sup>2+</sup> Titration Protocols To Quantify Proximal Al Sites in MFI.* Co<sup>2+</sup> ion exchange has been used to indicate the fraction of Al sites in close proximity to one another, yet the conditions reported to achieve saturated Co<sup>2+</sup> exchange of MFI samples vary widely among these literature reports (0.02–0.5 M Co<sup>2+</sup>, 298–353 K, 6–24 h, 1–3 sequential exchanges with fresh Co<sup>2+</sup> ion-exchange solutions).<sup>14,45,48,53–61</sup> Thus, we built on our prior work<sup>58</sup> to perform an extensive set of aqueous-phase Co<sup>2+</sup> ion-exchange experiments under a variety of conditions (i.e., temperature, molarity, time, number of sequential exchanges) to measure Co<sup>2+</sup> ion-exchange isotherms on Na-forms of a commercial MFI sample (MFI(13,C)) to determine when Co<sup>2+</sup> saturation was achieved (section S.7, SI). The resulting Co/Na-form MFI zeolites were characterized by a cation site balance to provide evidence for a 2:1 Co<sup>2+</sup> exchange stoichiometry at saturation (Figure S.20b, SI), which together with DRUV–vis spectra of the dehydrated Co/Na-MFI indicate that cobalt oxides are

absent (or present in minority amounts<sup>65</sup> relative to Co<sup>2+</sup> ions) on all Co-exchanged MFI samples (section S.8, SI); importantly, such spectra were not inappropriately used to identify or quantify distinct Co<sup>2+</sup> species.<sup>65</sup>

Our findings indicate that full Co<sup>2+</sup> titration of all available binding sites in MFI was only achieved from ion exchange performed at 353 K (section S.7, SI). In our hands, aqueous-phase Co<sup>2+</sup> ion exchange did not result in saturation of all binding sites in MFI at the commonly used ambient temperature conditions previously reported in the literature. This provides a reminder that Co-exchanged zeolites need to be prepared under varying exchange conditions and subsequently characterized by spectroscopic and titration methods to validate that Co<sup>2+</sup> saturation of all possible binding sites is achieved. This validation ensures that Co<sup>2+</sup> can be used as a quantitative titrant of proximal framework Al sites in a manner that can be reproduced by an independent laboratory and is agnostic to the specific method used to introduce Co<sup>2+</sup> ions to MFI samples. Thus, we conclude that quantitative interpretations regarding Al proximity in MFI zeolites may be inaccurate if Co<sup>2+</sup> ion exchange is performed at ambient temperatures or otherwise performed without the requisite spectroscopic and titration data to validate that Co<sup>2+</sup> saturation of all available binding sites been achieved. Our data indicate that saturation levels of Co<sup>2+</sup> ion exchange of MFI zeolites can be achieved at 353 K (section S.7, SI), which is taken as a functional estimate of the number of accessible proximal Al sites that serve as a favorable binding site for Co<sup>2+</sup> (herein referred to as paired Al sites). The difference between the number of H<sup>+</sup> sites on the parent H-MFI sample and the number of paired Al sites is taken as an estimate of the number of isolated framework Al sites.

Co<sup>2+</sup> titration was used to quantify the number of paired Al sites for MFI samples crystallized using only TPA<sup>+</sup> as the SDA (UV-vis spectra showing Co<sup>2+</sup> d-d transition bands without formation of cobalt oxides in section S.8, SI), which increased with the bulk Al content in the zeolite. Values of Co<sup>2+</sup>/Al<sub>tot</sub> were essentially undetectable on samples with dilute Al content in the limit of <1 per unit cell (Si/Al > 95), which contain predominantly isolated Al sites, and increased systematically over a range of ~10× as the Al content became more concentrated (1–2.5 Al per unit cell; Si/Al = 37–95). With increasing bulk Al content, the probability of siting two Al in close proximity is expected to increase.<sup>120</sup> Interestingly, a finite fraction of paired Al sites form on MFI samples with substoichiometric amounts of Al<sup>-</sup> relative to TPA<sup>+</sup> (Figure 7), as also reported previously (6–66% proximal Al, Si/Al = 29–60).<sup>45</sup>

The presence of a finite number of Co<sup>2+</sup>-titratable Al–Al pair sites on MFI zeolites crystallized using only an organic SDA (TPA<sup>+</sup>) contrasts our prior reports of CHA zeolites crystallized using only a bulky organic SDA (TMAda<sup>+</sup>).<sup>67</sup> In CHA zeolites, the use of TMAda<sup>+</sup> as the sole SDA results in negligible Co<sup>2+</sup> uptake, indicating that such protocols form zeolites with only isolated Al sites. Previous work has demonstrated that Co<sup>2+</sup> preferentially exchanges with proximal Al sites at the NNN or NNNN positions located within the 6-MR of CHA.<sup>52</sup> In contrast to CHA zeolites, the specific binding sites for Co<sup>2+</sup> in dehydrated states of MFI zeolites remain unclear,<sup>4</sup> and they cannot be identified in a straightforward manner by analyzing experimental DRUV-vis spectra. Thus, we turn to DFT to identify MFI lattice binding sites that are candidate hosts for bare Co<sup>2+</sup> ions and to

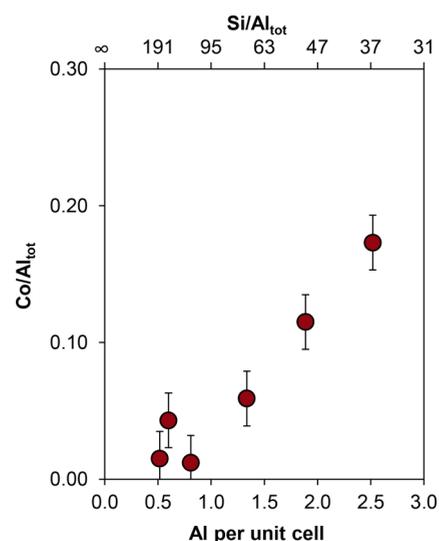


**Figure 7.** Co<sup>2+</sup>-saturation exchange levels on MFI crystallized only in the presence of TPA<sup>+</sup> as a function of framework Al content. Error bars represent ±0.02.

evaluate the properties of Al–Al pair configurations that endow favorable Co<sup>2+</sup> exchange energies. Importantly, the Al–Al site pairs that are evaluated next are a subset of all configurations with two TPA<sup>+</sup> cations (section 3.1.3); thus, they directly indicate that MFI zeolites crystallized only with TPA<sup>+</sup> can stabilize Al–Al pair configurations that are Co<sup>2+</sup> titratable.

**3.2.2. DFT Predictions of Co<sup>2+</sup> Binding Sites in MFI.** The specificity of Co<sup>2+</sup> titration has been established for CHA zeolites, in which Al–Al pairs within a 6-MR are selectively titrated by Co<sup>2+</sup> at both ambient (ca. 298 K) and elevated (353 K) temperatures (Figure S19, SI).<sup>52,67</sup> Such specificity should identify the range of plausible H<sup>+</sup>/Co<sup>2+</sup> exchange energies ( $\Delta E_{\text{Co-exch}}$ , eq 3) for which Co<sup>2+</sup> titration of Al–Al site pairs is likely to occur. Therefore, we first calculate Co<sup>2+</sup> exchange energies in CHA to benchmark those in MFI by examining Co<sup>2+</sup> cations exchanged into all possible proximal Al sites in NNN or NNNN arrangements or sharing 4-, 6-, and 8-MR in the CHA unit cell. We also optimized the H-form of each structure, examining all 16 possible O-site combinations for the pair of H<sup>+</sup>, from which Co<sup>2+</sup> exchange energies were calculated using eq 3. DFT-calculated Co<sup>2+</sup> exchange energies in CHA corroborate prior experimental<sup>67</sup> and theoretical<sup>52,121</sup> evidence, indicating that Co<sup>2+</sup> preferentially titrates two Al in an NNNN configuration ( $\Delta E_{\text{Co-exch}} = 38 \text{ kJ mol}^{-1}$ , Figure 8). The Co<sup>2+</sup> ion is 4-fold coordinated to O atoms in the 6-MR, consistent with similar reports of Co-form CHA (Figure S30, SI).<sup>52,122</sup> Two Al in NNN configurations have  $\Delta E_{\text{Co-exch}}$  values of 50 and 56 kJ mol<sup>-1</sup>, indicating that Co<sup>2+</sup> is slightly less stable than in NNNN environments, as also found in prior work.<sup>52</sup> All additional configurations tested have  $\Delta E_{\text{Co-exch}}$  values > 95 kJ mol<sup>-1</sup>, which are >40 kJ mol<sup>-1</sup> higher than the 6-MR Al–Al site pairs, consistent with results comparing Co-form energies (not exchange energies) in prior work.<sup>52</sup> On the basis of these Co<sup>2+</sup> exchange energies (Figure 8), sites that have  $\Delta E_{\text{Co-exch}} < 60 \text{ kJ mol}^{-1}$  are most likely to be titrated by Co<sup>2+</sup> and sites with  $\Delta E_{\text{Co-exch}} > 90 \text{ kJ mol}^{-1}$  are unlikely to be titrated; the threshold exchange energy (between 60 and 90 kJ mol<sup>-1</sup>) that dictates whether or not Co<sup>2+</sup> exchanges at the Al–Al site pair is unknown based on these data.

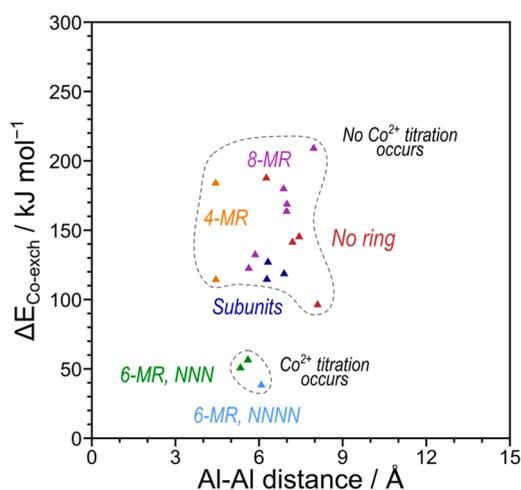


**Figure 8.** Energy to exchange two protons for one Co<sup>2+</sup> from Co(NO<sub>3</sub>)<sub>2</sub> (ΔE<sub>Co-exch</sub>, eq 3) at Al–Al pairs in CHA (▲) for pairs sharing 4-MR (orange), pairs sharing 6-MR and separated by 1 Si linker (6-MR NNN, green), pairs sharing 6-MR and separated by 2 Si linkers (6-MR NNNN, light blue), pairs sharing the di-6-MR and separated by 2 Si linkers (subunit, navy), and pairs sharing larger 8-MR (purple).

There are many proximal Al site motifs in MFI at which to examine H<sup>+</sup>/Co<sup>2+</sup> exchange: Al separated by short (<7 Å) distances that violate (Figure 9a) or do not violate Löwenstein's rule and are within small 4–6-MR (Figure 9b) or do not share rings (Figure 9c), or Al separated by large distances (>7 Å) (Figure 9d). These site motifs are likely to provide a dominant influence on the Co<sup>2+</sup> exchange behavior. Co<sup>2+</sup> exchanges into a 6-MR with an energy of 5 kJ mol<sup>-1</sup> (Figure 9b), while the other example structures within these motifs

exchanged Co<sup>2+</sup> with energies > 50 kJ mol<sup>-1</sup>. These examples suggest that, as in the case of CHA, Co<sup>2+</sup> prefers to exchange within small ring structures of MFI<sup>50</sup> where it can simultaneously interact with two Al<sup>-</sup> at short distances.

To systematically examine a range of likely Co<sup>2+</sup> exchange sites, we generated and optimized Co-form MFI for many Al–Al configurations. There are 612 distinct two-Al configurations in the 96 T-site orthorhombic MFI unit cell, accounting for symmetry; of those, we examined the 135 configurations that have Al–Al distances < 7 Å in which both Al<sup>-</sup> may simultaneously stabilize Co<sup>2+</sup>. We also optimized 67 two-Al configurations with Al–Al distances > 7 Å to examine the ability of Co<sup>2+</sup> to exchange Al–Al pairs within 10-MR structures, across intersections, or generally at larger distances. This resulted in a data set of 202 Co-form MFI structures. As with CHA, we optimized the 16 H-form structures for each of the 202 Al–Al pairs and computed ΔE<sub>Co-exch</sub> using eq 3. These Co<sup>2+</sup> exchange energies in MFI, when compared to those for CHA, were then used to suggest which Al site pair locations are likely (ΔE<sub>Co-exch</sub> < 60 kJ mol<sup>-1</sup>), possible (60–90 kJ mol<sup>-1</sup>), or unlikely (>90 kJ mol<sup>-1</sup>) to result in Co<sup>2+</sup> exchange.

Al–Al pairs in 6-MR and in NNNN arrangements have the lowest exchange energies (5–90 kJ mol<sup>-1</sup> and an average of 47 kJ mol<sup>-1</sup>; Figure 10b). This preference is the same as that found for CHA (Figure 8), confirming that 6-MR possesses the optimal size to host Co<sup>2+</sup> ions and that NNNN pairs provide a preferred environment for Co<sup>2+</sup> to coordinate with four O atoms associated with the two Al<sup>-</sup> tetrahedra. Not all 6-MR NNNN Al–Al pairs have ΔE<sub>Co-exch</sub> values < 60 kJ mol<sup>-1</sup> that represent likely exchange sites; of the 19 structures in this category, 12 have ΔE<sub>Co-exch</sub> < 60 kJ mol<sup>-1</sup> and the remaining 7 have ΔE<sub>Co-exch</sub> between 60 and 90 kJ mol<sup>-1</sup> (Table S7, S1), indicating that changes to the geometry of the 6-MR can engender a wide range in Co<sup>2+</sup> exchange energies, which may

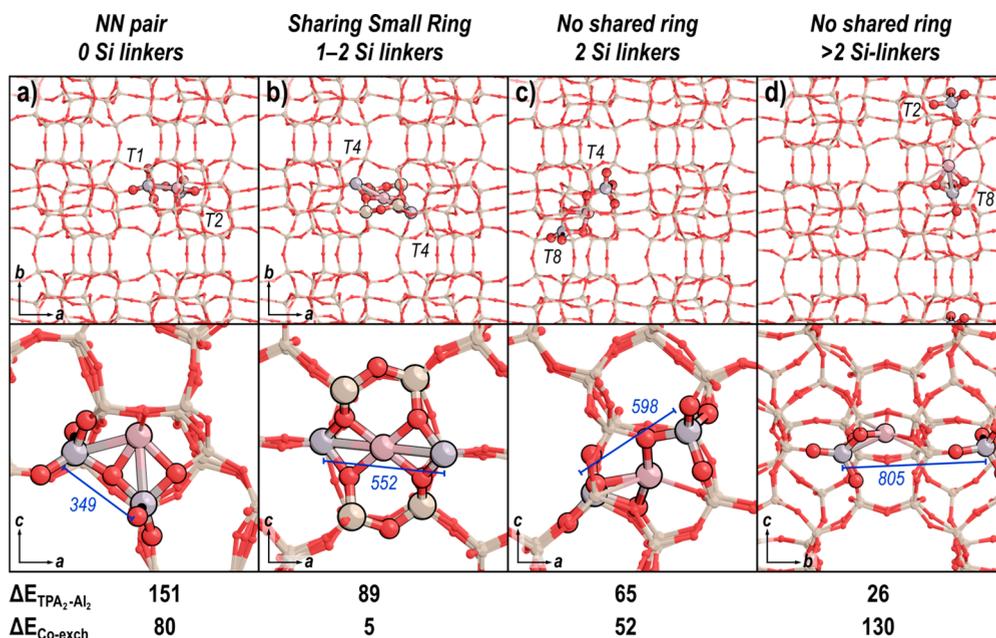


**Figure 9.** Al–Al pairs with the lowest ΔE<sub>Co-exch</sub> that (a) that violate Löwenstein's rule (NN pair), (b) share a 4-, 5-, or 6-MR, (c) are separated by 2 Si linkers but do not share a ring, and (d) are separated by >2 Si linkers and do not share a ring. Each structure is shown along the *c* vector of MFI (top) and in detail at the location of the Co<sup>2+</sup> (bottom). T-site identities of the Al in each structure are labeled in the top image, and Al–Al distance is shown in the bottom image in pm. Relative energy of the TPA form (ΔE<sub>TPA<sub>2</sub>-Al<sub>2</sub></sub>) and Co<sup>2+</sup> exchange energy (ΔE<sub>Co-exch</sub>) are shown in kJ mol<sup>-1</sup> beneath each structure.

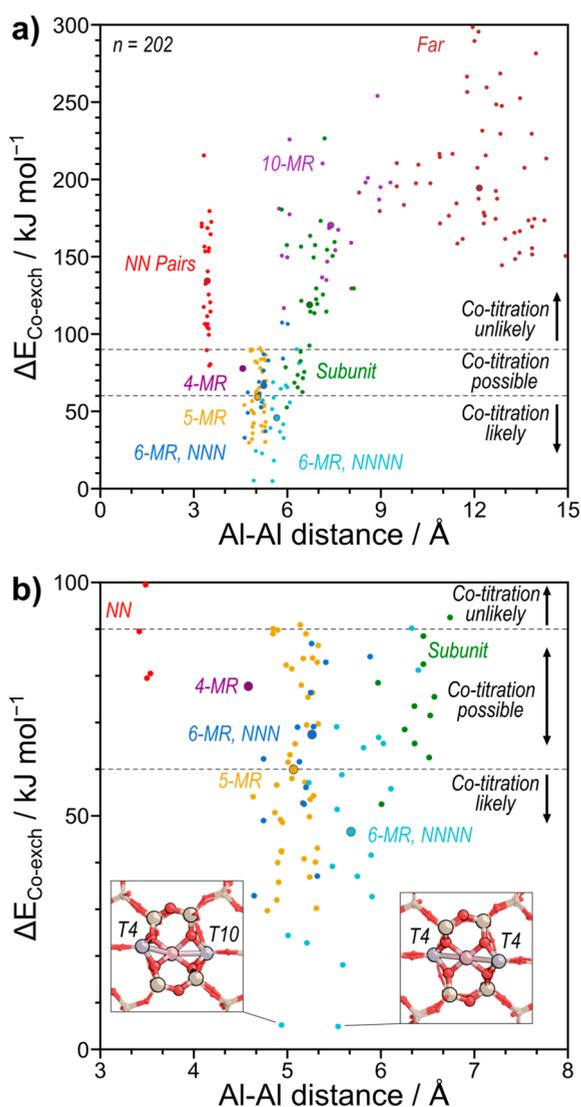


**Figure 10.** (a) Energy to exchange two protons for one  $\text{Co}^{2+}$  from  $\text{Co}(\text{NO}_3)_2$  ( $\Delta E_{\text{Co-exch}}$ , eq 3) at Al-Al pairs in MFI. Distinct exchange locations in MFI are shown separately: Al in NN arrangements (red), Al-Al pair sharing a 4-MR (dark purple), 5-MR (yellow), or 6-MR and separated by 1 Si linker (6-MR NNN, dark blue) or by 2 Si linkers (6-MR NNNN, light blue), Al-Al pairs sharing MFI subunits but no ring (Subunit, green), Al-Al pairs sharing 10-MR (light purple), and Al-Al pairs sharing no ring (Far, brown). Larger dots show average values within each set. (b) Detailed view of a, emphasizing sites where Co titration is most likely to occur. Two Al-Al pairs with the lowest  $\Delta E_{\text{Co-exch}}$  are shown with their Al locations labeled.

rationalize why  $\text{Co}^{2+}$  titration of MFI is far more sensitive to the exact conditions of experimental  $\text{Co}^{2+}$  ion exchange than CHA (section S7, SI).  $\Delta E_{\text{Co-exch}}$  values within the subset of 6-MR NNNN structures do not strongly correlate with O-Co-O angles, the perimeter formed by the four O atoms coordinated with the  $\text{Co}^{2+}$ , or Co-Al or Co-O distances. The two Al-Al pairs with the lowest  $\Delta E_{\text{Co-exch}}$  both include T4 sites (Figure 10b) and are located at NNNN positions in 6-MR of the *cas* subunit. Importantly, the distances between the Al in these pairs are shorter (5.52 and 4.91 Å for T4-T4 and T4-T10, respectively) than that found in the preferred 6-MR NNNN configuration in CHA (6.08 Å). Such proximity reduces  $\Delta E_{\text{Co-exch}}$  values further among these 6-MR NNNN

species, from 38  $\text{kJ mol}^{-1}$  in CHA to 5  $\text{kJ mol}^{-1}$  at these two Al-Al pairs in MFI.

$\text{Co}^{2+}$  exchange at Al in 6- and 5-MR at NNN positions is slightly less favorable with average  $\Delta E_{\text{Co-exch}}$  values of 68 and 61  $\text{kJ mol}^{-1}$ , respectively (Table S7, SI).  $\text{Co}^{2+}$  in these environments still coordinate to four O atoms attached to  $\text{Al}^-$  tetrahedra (Figure 11b and 11c); however, these environments do not solvate  $\text{Co}^{2+}$  as effectively as Al in 6-MR NNNN structures. There is only one unique 4-MR in MFI and, as such, only one site pair at a 4-MR NNN position that exchanges  $\text{Co}^{2+}$  with an energy of 77  $\text{kJ mol}^{-1}$ , which is higher than the average values for exchange at Al pairs in 5- and 6-MR (Figure 11a). Among the 80 Al pairs residing in NNN and NNNN arrangements within 4-, 5-, and 6-MR (structures shown in Figures S31–S36, SI), 42 (53%) have  $\Delta E_{\text{Co-exch}}$  values  $< 60 \text{ kJ mol}^{-1}$  corresponding to their likely titration and 34 (42%) have  $\Delta E_{\text{Co-exch}}$  values of 60–90  $\text{kJ mol}^{-1}$  that indicate possible titration, while only 5% have  $\Delta E_{\text{Co-exch}} > 90 \text{ kJ mol}^{-1}$  that indicate unlikely titration.

NN Al-Al pairs have higher  $\text{Co}^{2+}$  exchange energies than NNN or NNNN arrangements with an average  $\Delta E_{\text{Co-exch}}$  of 134  $\text{kJ mol}^{-1}$ . Only 3 of the 26 NN pairs (12%) have  $\Delta E_{\text{Co-exch}} < 90 \text{ kJ mol}^{-1}$ . Despite the proximity of the two  $\text{Al}^-$  to the  $\text{Co}^{2+}$  cation, exchange energies remain high because these NN Al-Al pairs do not surround the  $\text{Co}^{2+}$  with anionic charge as NNN and NNNN pairs often do, leading to unstable Co-form structures. This instability of Co forms coupled with the stability of NN pair H forms, previously shown in CHA,<sup>121</sup> result in high  $\Delta E_{\text{Co-exch}}$  values.

The 31 Al-Al pairs sharing MFI subunits without sharing a small ring have an average  $\Delta E_{\text{Co-exch}}$  value of 120  $\text{kJ mol}^{-1}$ ; only one such pair has  $\Delta E_{\text{Co-exch}} < 60 \text{ kJ mol}^{-1}$  (Figure 9c), while 9 (30%) had a value between 60 and 90  $\text{kJ mol}^{-1}$ , which indicate possible titration sites. The only arrangement in this motif with  $\Delta E_{\text{Co-exch}} < 60 \text{ kJ mol}^{-1}$  includes a T4 species, like the preferred  $\text{Co}^{2+}$  exchange locations in 6-MR NNNN Al-Al pairs. These data indicate that  $\text{Co}^{2+}$  is significantly less likely to titrate subunit Al pairs that do not also share a ring compared to those that do share a ring. Increasing separation distance and shared ring size further destabilize the Co-form, leading to concomitantly higher  $\Delta E_{\text{Co-exch}}$  values. All Al arrangements with Al-Al distances  $> 7 \text{ Å}$  have  $\Delta E_{\text{Co-exch}} > 90 \text{ kJ mol}^{-1}$  (Figure 10), further implicating structures with short Al-Al distances that share rings as the most probable hosts of  $\text{Co}^{2+}$  ions.

From these data we conclude that  $\text{Co}^{2+}$  prefers to titrate 5- and 6-MR within MFI, a finding that is seemingly consistent with the ring structures in MFI identified as dominant  $\text{Co}^{2+}$  binding sites in models developed previously by Dedecek and co-workers.<sup>15</sup> Of the 89 structures examined with  $\Delta E_{\text{Co-exch}} < 90 \text{ kJ mol}^{-1}$ , all but 13 are in a 5- or 6-MR, indicating that 85% of the structures likely or even possibly titrated by  $\text{Co}^{2+}$  are in these environments. Despite this preference for small rings, there is still a wider variety of possible binding sites that  $\text{Co}^{2+}$  can titrate in low-symmetry MFI than in CHA (where it binds selectively at NNN or NNNN sites in 6-MR). These small rings in MFI often comprise the walls of accessible pores, and we use this to define the environment (e.g., intersection or channel) of such pairs (Figure 12 and Table S6, SI). Notably, not all Al-Al pairs are directly accessible from these pore environments in the MFI topology. For example, some Al-Al pairs share a ring that spans a subunit connecting two pores and does not interface directly with an environment accessible

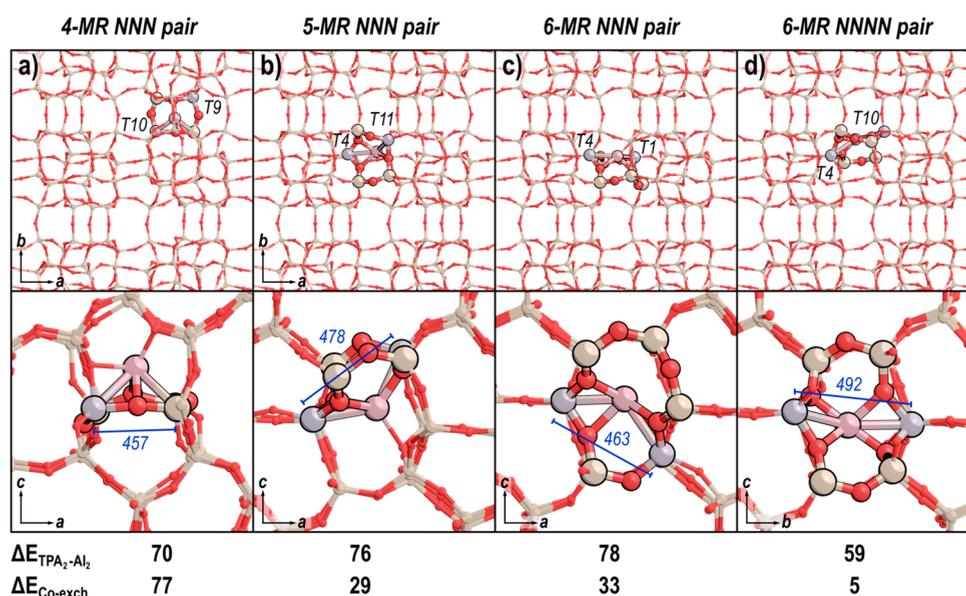


**Figure 11.** Al–Al pairs with the lowest  $\Delta E_{\text{Co-exch}}$  sharing (a) a 4-MR, (b) a 5-MR, (c) a 6-MR in a NNN configuration, and (d) Al–Al pair with the second lowest  $\Delta E_{\text{Co-exch}}$  sharing 6-MR in a NNNN configuration. Each structure is shown along the *c* vector of MFI (top) and in detail at the location of the  $\text{Co}^{2+}$  (bottom). T-site identities of the Al in each structure are labeled in the top image, and Al–Al distance is shown in the bottom image in pm. Relative energy of the TPA form ( $\Delta E_{\text{TPA}_2\text{-Al}_2}$ ) and  $\text{Co}^{2+}$  exchange energy ( $\Delta E_{\text{Co-exch}}$ ) are shown in  $\text{kJ mol}^{-1}$  beneath each structure.

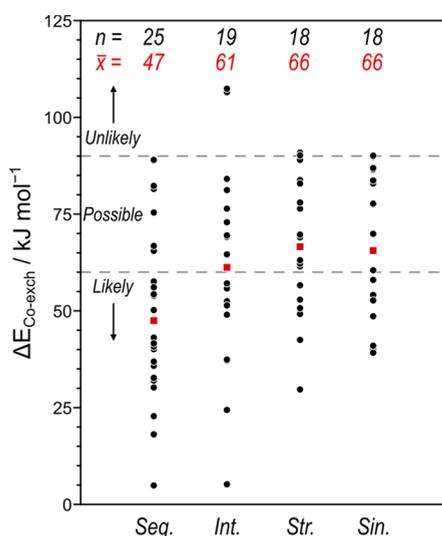


**Figure 12.**  $\text{Co}^{2+}$  exchange energies ( $\Delta E_{\text{Co-exch}}$ ) of Al–Al pairs in 4-, 5-, and 6-MR occupying different environments in MFI defined based on the accessibility of  $\text{Co}^{2+}$  to the micropore: sequestered from one location (Seq.), intersection (Int.), straight channel (Str.), and sinusoidal channel (Sin.).  $\text{Co}^{2+}$  binding sites are categorized as “likely” ( $\Delta E_{\text{Co-exch}} < 60 \text{ kJ mol}^{-1}$ ), “possible” ( $\Delta E_{\text{Co-exch}} = 60\text{--}90 \text{ kJ mol}^{-1}$ ), or “unlikely” ( $\Delta E_{\text{Co-exch}} > 90 \text{ kJ mol}^{-1}$ ) exchange sites. *n* indicates the number of unique Al–Al pairs in each location, and  $\bar{x}$  indicates the average  $\Delta E_{\text{Co-exch}}$  value among the *n* configurations at each location.

to larger guest molecules. These Al–Al pairs sharing rings that span subunits are treated distinctly from Al–Al pairs that share subunits but not rings. These sequestered rings (25 pairs; Figure 12) have the lowest average  $\Delta E_{\text{Co-exch}}$  value ( $47 \text{ kJ mol}^{-1}$ ) of any environment in which Al–Al pairs may be accessed and the largest percentage of possible pairs that are likely hosts of  $\text{Co}^{2+}$  based on  $\Delta E_{\text{Co-exch}}$  (76%). Despite this moniker, sequestered  $\text{Co}^{2+}$  sites may still be titrated; here, we are simply reporting that the  $\text{Co}^{2+}$  is centered within a subunit

of MFI (e.g., the *cas* subunit for Figure 9b). Al–Al pairs that are located at the interface with channel intersections produce some similarly preferred structures with low  $\text{Co}^{2+}$  exchange energies, but some Al–Al pairs sharing small rings in these environments are also unlikely  $\text{Co}^{2+}$  exchange locations. This leads to a higher average exchange value for Al–Al pairs in intersections than for sequestered pairs. Finally, Al–Al pairs that are located on the walls of the straight or sinusoidal channel have the largest average exchange values ( $\Delta E_{\text{Co-exch}} = 66$  and  $66 \text{ kJ mol}^{-1}$ , respectively) but much smaller ranges of exchange energies ( $29\text{--}91$  and  $39\text{--}90 \text{ kJ mol}^{-1}$ , respectively). These data indicate that stable  $\text{Co}^{2+}$  binding sites are distributed widely among the various environments of MFI, but many are located in subunits that are not directly accessible without first requiring  $\text{Co}^{2+}$  diffusion through 5- or 6-MR, which may rationalize the higher  $\text{Co}^{2+}$  titration values achieved at higher exchange temperatures (353 K; section 3.2.1).

In summary, we have fully characterized the types of sites (predominantly Al sharing 5- and 6-MR) that may be observed by experimental  $\text{Co}^{2+}$  titration methods, indicating that many Al–Al pair configurations present in all void environments in MFI are likely to be titrated by  $\text{Co}^{2+}$ . However, our calculations indicate that many of these two-Al structures are unfavorable in the presence of  $\text{TPA}^+$  because of their short Al–Al distances, which generally result in less stable ionic arrangements. Indeed, only a small fraction of the Al–Al pairs that give exchange energies  $< 90 \text{ kJ mol}^{-1}$  (6% of 89) have  $\text{TPA}_2\text{-Al}_2$  structures within  $40 \text{ kJ mol}^{-1}$  of the most stable arrangement with an additional 58% having relative  $\text{TPA}_2\text{-Al}_2$  energies  $< 80 \text{ kJ mol}^{-1}$ . These large relative  $\text{TPA}_2\text{-Al}_2$  indicate that such Al arrangements are unlikely to form if the  $\text{TPA}_2\text{-Al}_2$  calculations faithfully represent synthesis conditions (Table 4). Critically, Al siting during MFI synthesis depends on a mixture of thermodynamics and kinetics, the latter of which is not considered in this initial probe of the  $\text{TPA}_2\text{-Al}_2$  energy landscape. Furthermore, the  $\text{TPA}^+$  content in these DFT calculations is lower (2  $\text{TPA}^+$  per MFI unit cell)

**Table 4. Number of Structures That Are Likely,<sup>a</sup> Possible,<sup>b</sup> or Unlikely<sup>c</sup> To Be Titrated by Co<sup>2+</sup> and Structures with Low, Intermediate, and High TPA-Form Energies**

$\Delta E_{\text{Co-exch}}$ category	TPA-form energy, $\Delta E_{\text{TPA}^+ - \text{Al}_2}$		
	Low <40 kJ mol <sup>-1</sup>	Intermediate 40–80 kJ mol <sup>-1</sup>	High >80 kJ mol <sup>-1</sup>
likely <sup>a</sup>	3	26	14
possible <sup>b</sup>	2	26	18
unlikely <sup>c</sup>	19	61	33

<sup>a</sup> $\Delta E_{\text{Co-exch}} < 60$  kJ mol<sup>-1</sup>. <sup>b</sup> $\Delta E_{\text{Co-exch}} < 60$ –90 kJ mol<sup>-1</sup>. <sup>c</sup> $\Delta E_{\text{Co-exch}} > 90$  kJ mol<sup>-1</sup>.

than observed by TGA in experimentally synthesized samples (~4 TPA<sup>+</sup> per MFI unit cell, Figure 1), and the presence and role of defect siloxy (SiO<sup>-</sup>) groups was not considered. In addition, the presence of solvent and additional ionic species in and around the framework is likely to reduce the degree to which Al arrangements with large Al–Al distances are favored, as discussed in section 3.1.3. The presence of up to 34% of Al<sup>-</sup> in Co<sup>2+</sup>-titratable locations in TPA-only MFI syntheses (Table 1) indicates that kinetic factors during crystallization, the presence of a solvent, and the formation of defect sites may play a major role in screening the Coulombic interactions that are captured in our calculations and seek to bias Al siting in isolated positions.

**3.3. Influence of TPA<sup>+</sup> and Na<sup>+</sup> co-SDAs on Al Proximity in MFI.** We next study the influence of using different SDAs and their combinations on the number of isolated and paired Al sites formed in MFI zeolites. First, synthesis gels were prepared to contain varying amounts of Na<sup>+</sup> (Na<sup>+</sup>/TPA<sup>+</sup> = 0.25–5), an inorganic cation with a higher charge density than TPA<sup>+</sup>, while holding constant the total cationic charge ((Na<sup>+</sup> + TPA<sup>+</sup>)/Al = 30) and Al content (Si/Al = 50). Crystalline MFI products were obtained with essentially constant Si/Al = 50–57 with XRD patterns (Figure S2, SI) and micropore volumes consistent with the MFI topology (0.12–0.15 cm<sup>3</sup> g<sup>-1</sup>, Table 1, Figure S6, SI). The Na<sup>+</sup> content on the as-made MFI samples was measured by elemental analysis, and the TPA<sup>+</sup> content was calculated from organic weight loss measured by TGA. Both of these values are plotted in Figure 13 along with the total cation (Na<sup>+</sup> + TPA<sup>+</sup>) content with the data for the MFI-TPA(50,0) sample (Figure 1) crystallized using only TPA<sup>+</sup> also plotted for comparison.

Interestingly, addition of Na<sup>+</sup> to the synthesis gel crystallized MFI zeolites with ~5 cations occluded per unit cell (Figure 13, filled circles) for the entire gel composition studied here (Na<sup>+</sup>/TPA<sup>+</sup> = 0.25–5), which sharply contrasts the 4 TPA<sup>+</sup> cations occluded per unit cell for the TPA-only suite of MFI samples (Figure 1). As the Na<sup>+</sup>/TPA<sup>+</sup> present in the synthesis gel increased from 0.25 to 5, the occluded TPA<sup>+</sup> content generally decreased from ~4 to ~3.2 per unit cell (Figure 13, open squares), while the occluded Na<sup>+</sup> content generally increased from ~1.1 to ~2.3 per unit cell (Figure 13, filled gray squares), consistent with prior reports.<sup>48</sup> All zeolite products crystallized under these conditions contained at least 1 Na<sup>+</sup> per unit cell, and the relative amounts of co-occluded TPA<sup>+</sup> and Na<sup>+</sup> (>5 per unit cell) indicate that Na<sup>+</sup> does not fully compete with TPA<sup>+</sup> for occupancy in MFI channel intersections. Rather, Na<sup>+</sup> likely first occludes within the smaller channels of MFI as previously hypothesized<sup>46–48</sup> and only appears to begin replacing TPA<sup>+</sup> at a higher Na<sup>+</sup> content in the gel (>0.75 Na<sup>+</sup>/TPA<sup>+</sup><sub>gel</sub>). At higher Na<sup>+</sup> contents in the synthesis gel, it is

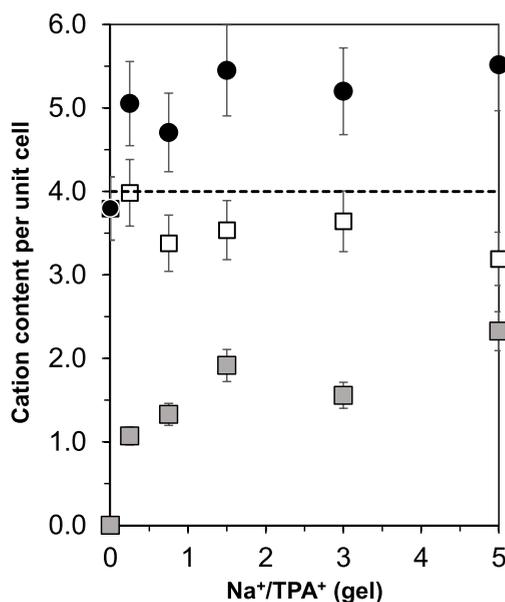


**Figure 13.** Occluded TPA<sup>+</sup> content as measured by TGA on the series of MFI (Si/Al<sub>gel</sub> = 50, Na<sup>+</sup>/TPA<sup>+</sup><sub>gel</sub> = 0–5, open squares). Na<sup>+</sup> content measured by elemental analysis on the solid crystalline product after washing and oxidative treatment (gray squares). Total cation content (Na<sup>+</sup> + TPA<sup>+</sup>, filled circles) also shown for reference. Dashed line corresponds to 1 TPA<sup>+</sup> per MFI channel intersection (96 T-site unit cell). Error bars are ±10%.

possible that Na-rich phases of MFI may crystallize given prior reports that MFI can crystallize using only Na<sup>+</sup> as the SDA.<sup>123–127</sup>

The fraction of paired Al as measured by Co<sup>2+</sup> titration (DRUV-vis spectra in section S.8, SI) is plotted in Figure 14 for the MFI samples crystallized with 5 cations occluded per unit cell (using Na<sup>+</sup> and TPA<sup>+</sup> as co-SDAs, Figure 13) and generally increased with the amount of Na<sup>+</sup> retained on the crystalline MFI product (Figure 14, filled squares). The occlusion of larger amounts of higher charge-density cations (e.g., Na<sup>+</sup>) has previously been attributed to incorporate more Al into zeolite structures,<sup>106–108</sup> which in turn should increase Al–Al proximity on average.<sup>120</sup> Importantly, the samples studied here were purposefully synthesized to restrict the total Al content to an essentially constant value (Si/Al = 50) as more Na<sup>+</sup> was incorporated within the crystalline MFI products (Figure S16, SI), indicating that Na<sup>+</sup> co-occlusion with TPA<sup>+</sup> influences Al proximity. Recently, we combined experimental material synthesis and characterization together with DFT calculations and Monte Carlo simulations to provide evidence that Na<sup>+</sup> co-occludes with the OSDA (TMAda<sup>+</sup>) in CHA to favor formation of proximal Al sites (2 Al in 1 6-MR).<sup>52</sup> Applying these same computational approaches to investigate the influence of Na<sup>+</sup> and TPA<sup>+</sup> in the MFI unit cell on Al distribution is intractable here given the diverse configurational space of lattice binding sites and SDA configurations and the presence of lattice defects that could also balance these cations. We surmise, however, that Na<sup>+</sup> may similarly promote formation of paired Al configurations when co-occluded with TPA<sup>+</sup> in the MFI unit cell, as it does when co-occluded with TMAda<sup>+</sup> in the CHA unit cell. As a point of reference, the data point for MFI-TPA(50,0) is also plotted in Figure 14 (gray triangle); however, this sample should not be expected to behave according to the synthesis–structure

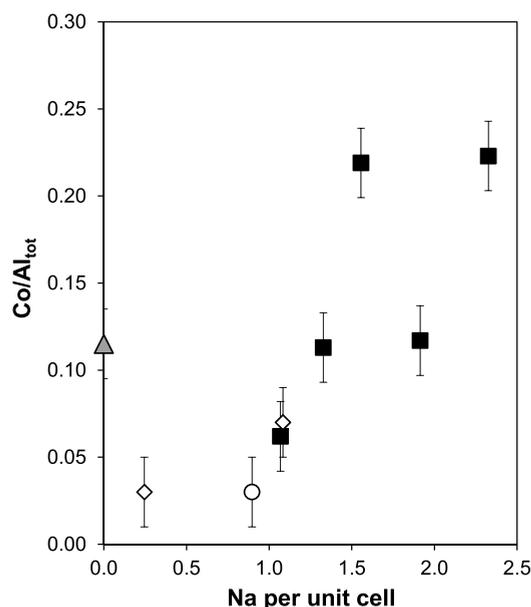


**Figure 14.** Dependence of the number of Al–Al pairs titrated by  $\text{Co}^{2+}$  among MFI samples of similar Si/Al ratio (43–58) on the  $\text{Na}^+$  content retained on the crystalline product for the samples synthesized with PETP ( $\circ$ ), DABCO ( $\diamond$ ), and  $\text{TPA}^+$  ( $\blacksquare$ ) as the primary OSDA. MFI-TPA(50,0) is also shown (gray triangle) but contains 4 SDA cations occluded per unit cell in the synthesized form (Figure 13) and thus should behave according to a different synthesis–structure relation than the Na-containing TPA samples that contain 5 SDA cations occluded per unit cell in the synthesized form (Figure 13). Error bars are  $\pm 10\%$ .

relation for the MFI samples synthesized with a mixture of  $\text{Na}^+$  and  $\text{TPA}^+$  because it contains 4 SDA cations occluded per unit cell, while the latter suite of samples contains 5 (Figure 13), which likely influences the energies to form different framework Al–Al arrangements given the sensitivity of such energies to electrostatic interactions (Figure 2).

**3.4. Influence of Neutral Organics and  $\text{Na}^+$  co-SDAs on Al Proximity in MFI.** We hypothesized that using charge-neutral OSDAs should occlude intraporous void spaces without providing charge compensation for framework Al centers, thereby influencing Al proximity differently than when using cationic  $\text{TPA}^+$  as the OSDA. To study the effects of using charge-neutral OSDAs together with  $\text{Na}^+$  in zeolite synthesis media on the resulting Al distribution in MFI, we performed two sets of synthesis experiments to crystallize MFI samples of similar Si/Al ratio as the MFI-TPA(50,Y) series but using either PETP or a mixture of DABCO and methylamine (Scheme 1). The zeolite products from these crystallization experiments were consistent with the MFI framework topology (XRD patterns, micropore volumes, and  $^{27}\text{Al}$  MAS NMR spectra in sections S.1–S.3, SI).

In the case of PETP as the charge-neutral OSDA, a recipe adapted from Park et al.<sup>68</sup> using a  $\text{Na}^+/\text{PETP}$  of 0.5 in the synthesis media resulted in crystallizing a solid MFI product with Si/Al = 43 (MFI-PETP(43,0.5), Table 1). We note that the lower than expected micropore volume ( $0.11 \text{ cm}^3 \text{ g}^{-1}$ , Table 1;  $0.13 \text{ cm}^3 \text{ g}^{-1}$  reported by Park et al.<sup>68</sup>) and some broad features in the XRD pattern ( $2\theta = 32\text{--}40^\circ$ , Figure S3, SI) suggest that this MFI sample may not be fully crystalline and may contain some amorphous domains. The MFI-

PETP(43,0.5) sample contained approximately 1  $\text{Na}^+$  per unit cell (Figure 14), similar to the MFI-TPA(52,0.25) sample, yet contained less than one-half the amount of OSDA per unit cell (1.95 PETP per unit cell Table S2, section S.5, SI), similar to previous reports (2.4 PETP per unit cell).<sup>48,68</sup> These findings suggest that PETP, unlike  $\text{TPA}^+$ , only occupies one-half of the intersections in MFI on average. The MFI-PETP(43,0.5) sample also had a lower fraction of proximal Al ( $\text{Co}/\text{Al}_{\text{tot}} = 0.03$ , Figure 14) than any of the MFI-TPA samples of similar bulk Si/Al. This result may be rationalized by considering PETP to behave as a charge-neutral molecule that occupies intraporous void spaces<sup>48,68</sup> and separates occluded cationic species (including  $\text{Na}^+$ ) at larger average distances relative to one another, which may facilitate the separation of framework Al centers.

We also performed two replicate crystallization experiments using DABCO as the primary charge-neutral OSDA with synthesis solutions of nominally identical composition ( $\text{Na}^+/\text{DABCO} = 0.04$ ) that contained  $\text{Na}^+$  and a mixture of DABCO and methylamine. These two replicate samples, referred to as MFI-DABCO(44,0.04)-1 and MFI-DABCO(44,0.04)-2, resulted in crystallizing a solid MFI product with Si/Al = 44 (Table 1). Previous reports have indicated that DABCO alone does not behave as an OSDA for MFI<sup>126</sup> but that it can be derivatized to prepare organic molecules that do behave as OSDAs for MFI;<sup>128,129</sup> thus, crystallization of MFI using DABCO as an organic reagent (albeit with another organic molecule, methylamine, also present) was unexpected. TGA estimates of the OSDA per unit cell (4.24 and 3.69 OSDA per unit cell for samples –1 and –2, respectively, Table S2, section S.5, SI) indicate that each MFI intersection was filled with one DABCO molecule, suggesting that it is more efficient at occluding intraporous void spaces than PETP, and behaves similarly to  $\text{TPA}^+$ . The two replicate DABCO-assisted MFI synthesis experiments, however, resulted in differences in the amount of occluded  $\text{Na}^+$  on the crystalline solids (Figure 14) with one sample with significantly lower  $\text{Na}^+$  content (0.25  $\text{Na}$  per unit cell, Figure 14) than measured on any of the MFI-TPA+ samples. These findings are consistent with our prior work on crystallization of CHA zeolites in which replicate crystallization experiments using a synthesis medium with a given  $\text{Na}^+$  content may result in crystallization of solid zeolite phase with varying  $\text{Na}^+$  content.<sup>52,67</sup> Interestingly, the fraction of proximal Al formed on the DABCO-assisted MFI materials shows a positive correlation with the amount of  $\text{Na}^+$  occluded on the solid products (Figure 14), similar to the MFI-TPA series (Figure 14). The  $\text{Na}^+/\text{OSDA}$  ratios used in the synthesis media to crystallize an MFI product with a specific amount of occluded  $\text{Na}^+$  per unit cell (e.g.,  $\sim 1$ ; Figure 14) was significantly lower for the case of DABCO (0.04) than  $\text{TPA}^+$  (0.25–5), illustrating that crystallizing MFI zeolites with a targeted amount of proximal Al sites can require different relative amounts of inorganic and organic SDAs in the synthesis mixture, providing opportunities to design routes that do so while minimizing OSDA usage if so desired.

The data in Figure 14 reflect MFI samples of similar bulk Al content (Si/Al = 43–58), allowing for direct comparisons of the influence of cationic ( $\text{TPA}^+$ ) and charge-neutral (PETP, DABCO) OSDAs when used together with  $\text{Na}^+$  as an inorganic co-SDA. The  $\text{Na}^+$  content occluded in the solid MFI products crystallized using cationic and charge-neutral co-SDAs generally correlated to the amount of proximal Al–Al site pairs formed (Figure 14). Such low contents of occluded



Na<sup>+</sup> in MFI crystallized using charge-neutral OSDAs (<1 per unit cell, Figure 14) are typically not observed in literature (3.8–4.8 Na per unit cell);<sup>48</sup> however, commonly reported synthesis mixtures are intended to crystallize samples with higher Al content, which may require occluding more Na<sup>+</sup> in crystalline solids. We hypothesize the lower fraction of paired Al–Al in the neutral OSDA MFI samples, compared to the MFI-TPA series, indicates that cationic charge centers (e.g., Na<sup>+</sup>) were spatially separated at larger average distances in intraporous void spaces, thereby separating the anionic Al<sup>−</sup> in the framework.

Finally, we note that the presence of a finite number of Co<sup>2+</sup>-titratable Al–Al pair sites on MFI zeolites crystallized using only TPA<sup>+</sup> at an Si/Al = 50 (24% Al in proximal configurations, Table 1) or with TPA<sup>+</sup> and Na<sup>+</sup> at similar composition (Si/Al = 50–58, 12–44% Al in proximal configurations, Table 1) provides a sharp contrast to our prior report of using mixtures of TPA<sup>+</sup> and ethylenediamine (EDA) to crystallize B-Al-MFI materials of similar composition (Si/Al ≈ 50) but with undetectable amounts of Co<sup>2+</sup>-titratable Al–Al pair sites (<5% Al in proximal configurations, Hur et al., Figure 4).<sup>58</sup> In our prior B-Al-MFI synthesis work, we proposed that complexes formed between two B heteroatoms and one EDA become occluded within microporous voids of MFI, competing with the occlusion of TPA<sup>+</sup> so as to cause its dilution within the crystallizing framework and the siting of framework Al at larger average distances.<sup>58</sup> The occlusion of a space-filling organic moiety (PETP, DABCO) or an organic–inorganic complex (2B-EDA), which may site B atoms in the lattice that are unable to compensate for Co<sup>2+</sup> or generate proton sites as strong as those generated by Al<sup>−</sup>,<sup>58</sup> appears to provide a similar influence on the ability to spatially separate framework Al and associated H<sup>+</sup> active sites that are relevant for most Brønsted acid-catalyzed reactions.

#### 4. CONCLUSIONS

Given the emerging recognition that using mixtures of structure-directing agents (SDAs) of different molecular structure and cationic charge is a promising route to influence Al siting and substitution patterns in zeolite frameworks, we explored this concept for MFI zeolites to identify synthesis–structure relations that can describe how different SDAs and SDA mixtures influence Al proximity in MFI. In contrast to high-symmetry frameworks such as CHA, efforts to first define and then quantify Al–Al site pairs in MFI zeolites are impeded by the combinatorial complexity resulting from its low-symmetry framework (12 unique T-sites), which generates 13 680 unique arrangements of TPA<sub>2</sub>–Al<sub>2</sub> structures in a 96 T-site MFI unit cell. DFT calculations for 1 framework Al<sup>−</sup> site and occluded TPA<sup>+</sup> cation reveal the dominant influence of N<sup>+</sup>–Al<sup>−</sup> electrostatic interactions on lattice Al-siting energies. This finding allowed enforcing a rough N<sup>+</sup>–Al<sup>−</sup> distance cutoff criterion of < 6.5 Å to reduce the number of TPA<sub>2</sub>–Al<sub>2</sub> pair configurations by nearly an order of magnitude to identify 1773 possible Al–Al pair configurations formed by TPA<sup>+</sup> to exhaustively study by DFT to examine TPA–Al, Al–Al, and Al<sub>2</sub>–Co interactions. Al–Al site pairs in shared ring structures, most commonly in the 5-MR and 6-MR, provide 43 different configurations (including all of the 12 symmetrically unique T-sites) that can favorably host Co<sup>2+</sup> ions, rationalizing the observation that a finite fraction of Al–Al pairs form in MFI when using TPA<sup>+</sup> as the sole SDA, revealing the diverse range

of Al–Al pair configurations that may be quantified by experimental Co<sup>2+</sup> titration.

Experimental protocols to reproducibly quantify Al–Al site pairs on MFI zeolites using aqueous Co<sup>2+</sup> ion exchange have remained imprecisely described in the literature and vary widely among prior reports. This required us to perform extensive experimentation to develop an experimental Co<sup>2+</sup> titration protocol for MFI zeolites (aqueous ion exchange with 0.5 M Co(NO<sub>3</sub>)<sub>2</sub> for 24 h at 353 K on Na-form MFI samples), validated by spectroscopic and site balance data to confirm that Co<sup>2+</sup> saturation uptakes have been achieved. Importantly, diffuse reflectance UV–vis spectroscopy can only be used as a qualitative characterization method to confirm that absorbance features for Co<sup>2+</sup> d–d transitions are present and those for Co–oxides are absent, and it cannot be used in a straightforward manner to distinguish or quantify various Co<sup>2+</sup> binding site environments, given the finite temperature restructuring of transition metal ions in (alumino)siloxane rings that give rise to multiple coordination complexes (and d–d transitions, in turn) even for a single ion site in a single X-MR. The lack of a robust experimental method to reliably quantify Al–Al site pairs in MFI frameworks or any zeolite framework in general will confuse efforts that attempt to develop synthesis–structure relations that describe how SDAs influence Al proximity.

MFI zeolites crystallized using only tetrapropylammonium (TPA<sup>+</sup>) as the sole organic SDA resulted in samples with varying Al content (Si/Al = 37–180; 0.52–2.52 Al per unit cell), as expected from the occlusion of one TPA<sup>+</sup> per MFI channel intersection and with predictions from charge density mismatch theory. Such MFI samples contained fractions of Al in paired configurations (0–34%) that increased systematically with Al content, consistent with DFT predictions that 2 TPA<sup>+</sup> cations can charge-compensate Al–Al site pairs that are in these arrangements with N<sup>+</sup>–Al<sup>−</sup> distances < 6.5 Å. These findings rationalize previous reports<sup>45</sup> indicating that finite fractions of Al–Al site pairs can form in MFI zeolites crystallized using only TPA<sup>+</sup>. They also provide a striking contrast to our previous report of using mixtures of TPA<sup>+</sup> and ethylenediamine to crystallize B-Al-MFI materials of similar bulk Al content (Si/Al ≈ 50)<sup>58</sup> but with undetectable amounts of Al–Al site pairs titratable by Co<sup>2+</sup>; MFI zeolites of such Al arrangement and composition were not accessible using only TPA<sup>+</sup> and Al as the framework heteroatom under the synthesis conditions studied in this work.

The use of mixtures of cationic (TPA<sup>+</sup>) or charge-neutral (PETP, DABCO) OSDAs, together with Na<sup>+</sup> as a co-SDA, crystallized MFI zeolites with similar Al content (Si/Al ≈ 50) but with fractions of Al in paired configurations (6–44%) that generally increased with the co-occluded Na<sup>+</sup> content retained on the crystalline solids. This correlation constitutes a synthesis–structure relation that resembles and extends our prior relation for CHA zeolites using mixtures of TMAda<sup>+</sup> and Na<sup>+</sup> cations to systematically vary Al–Al site pairing at fixed composition.<sup>52,67</sup> Replacement of TPA<sup>+</sup> with charge-neutral OSDAs (PETP, DABCO), intended to occupy void space without providing the capacity to charge-compensate framework Al<sup>−</sup>, resulted in forming fewer numbers of Al–Al pairs without altering the total Al content, suggesting that charge-neutral molecules can be exploited to occupy microporous voids during crystallization to bias toward forming isolated framework Al sites. We expect that the methodology described herein, combining DFT calculations of SDA–Al<sup>−</sup> interactions

to suggest Al-siting preferences and titrant exchange energies to determine structural criteria can be applied to provide a reasonable number of candidate Al pairs detected in an experimental material, can be adapted for other SDAs and framework topologies. These findings also highlight how experiment and theory can be combined to develop robust Al–Al proximity models in zeolites that can be exercised to interrogate samples synthesized using different SDAs and SDA combinations in order to aid in developing synthetic strategies that crystallize zeolites with varying framework Al arrangements, even at fixed bulk Al composition (if so desired), to engineer changes in their catalytic and adsorption properties.

## ■ ASSOCIATED CONTENT

### SI Supporting Information

The Supporting Information is available free of charge at <https://pubs.acs.org/doi/10.1021/acs.chemmater.0c03154>.

XRD patterns, N<sub>2</sub> adsorption isotherms, <sup>27</sup>Al MAS NMR, NH<sub>3</sub> titration and TPD, TGA, elemental analysis, discussion of the aqueous-phase Co<sup>2+</sup> ion-exchange procedure, DRUV–vis spectra, MFI O-atom environments, DFT calculations for TPA-form MFI with 1–2 Al, DFT calculations of Co<sup>2+</sup> exchange in CHA and MFI (PDF)

## ■ AUTHOR INFORMATION

### Corresponding Authors

**David D. Hibbitts** – Department of Chemical Engineering, University of Florida, Gainesville, Florida 32611, United States; [orcid.org/0000-0001-8606-7000](https://orcid.org/0000-0001-8606-7000); Email: [hibbitts@che.ufl.edu](mailto:hibbitts@che.ufl.edu)

**Rajamani Gounder** – Charles D. Davidson School of Chemical Engineering, Purdue University, West Lafayette, Indiana 47907, United States; [orcid.org/0000-0003-1347-534X](https://orcid.org/0000-0003-1347-534X); Email: [rgounder@purdue.edu](mailto:rgounder@purdue.edu)

### Authors

**Claire T. Nimlos** – Charles D. Davidson School of Chemical Engineering, Purdue University, West Lafayette, Indiana 47907, United States

**Alexander J. Hoffman** – Department of Chemical Engineering, University of Florida, Gainesville, Florida 32611, United States

**Young Gul Hur** – Charles D. Davidson School of Chemical Engineering, Purdue University, West Lafayette, Indiana 47907, United States

**Byung Jin Lee** – Charles D. Davidson School of Chemical Engineering, Purdue University, West Lafayette, Indiana 47907, United States; Department of Chemical and Biological Engineering, Korea University, Seongbuk-gu, Seoul 02841, Republic of Korea

**John R. Di Iorio** – Charles D. Davidson School of Chemical Engineering, Purdue University, West Lafayette, Indiana 47907, United States; [orcid.org/0000-0002-7519-5100](https://orcid.org/0000-0002-7519-5100)

Complete contact information is available at: <https://pubs.acs.org/10.1021/acs.chemmater.0c03154>

### Author Contributions

§C.T.N. and A.J.H. contributed equally to this work.

### Notes

The authors declare no competing financial interest.

## ■ ACKNOWLEDGMENTS

For the experimental work at Purdue, we acknowledge financial support provided by the National Science Foundation CAREER program under award number 1552517-CBET for the study of MFI samples prepared using cationic OSDAs (TPA<sup>+</sup>) and the National Science Foundation under Cooperative Agreement No. EEC-1647722, which is an Engineering Research Center for the Innovative and Strategic Transformation of Alkane Resources for the study of MFI samples prepared using charge-neutral cationic OSDAs (PETP, DABCO). We acknowledge the BK21Plus Program (21A20131812182) funded by the Ministry of Education (MOE, Korea) and the National Research Foundation of Korea (NRF) for supporting the visiting scholar appointment for B.J.L. at Purdue. We thank Elizabeth E. Bickel (Purdue) for helpful technical discussions and a critical review of this manuscript. We also thank Dr. John Harwood (Purdue Interdepartmental NMR Facility) for assistance with solid-state NMR and Sachem, Inc. for providing the organic structure-directing agent used to synthesize SSZ-13. For the computational work at the University of Florida, we acknowledge support from the National Science Foundation CAREER program under award 1942684-CBET. This work used the Extreme Science and Engineering Discovery Environment (XSEDE),<sup>130</sup> which is supported by the National Science Foundation grant number ACI-1548562 through allocation CTS160041.

## ■ REFERENCES

- (1) Baerlocher, C.; McCusker, L. B. Database of Zeolite Structures <http://www.iza-structure.org/databases/> (accessed Jul 31, 2020).
- (2) First, E. L.; Gounaris, C. E.; Wei, J.; Floudas, C. A. Computational Characterization of Zeolite Porous Networks: An Automated Approach. *Phys. Chem. Chem. Phys.* **2011**, *13* (38), 17339–17358.
- (3) Haag, W. O.; Lago, R. M.; Weisz, P. B. The Active Site of Acidic Aluminosilicate Catalysts. *Nature* **1984**, *309* (5969), 589–591.
- (4) Knott, B. C.; Nimlos, C. T.; Robichaud, D. J.; Nimlos, M. R.; Kim, S.; Gounder, R. Consideration of the Aluminum Distribution in Zeolites in Theoretical and Experimental Catalysis Research. *ACS Catal.* **2018**, *8* (2), 770–784.
- (5) Gounder, R.; Iglesia, E. Catalytic Consequences of Spatial Constraints and Acid Site Location for Monomolecular Alkane Activation on Zeolites. *J. Am. Chem. Soc.* **2009**, *131* (5), 1958–1971.
- (6) Haag, W. O. Catalysis by Zeolites – Science and Technology. In *Studies in Surface Science and Catalysis*; Weitkamp, J., Karge, H. G., Pfeifer, H., Hölderich, W., Eds.; Elsevier: Amsterdam, 1994; Vol. 84, pp 1375–1394.
- (7) Jones, A. J.; Iglesia, E. The Strength of Brønsted Acid Sites in Microporous Aluminosilicates. *ACS Catal.* **2015**, *5* (10), 5741–5755.
- (8) Gounder, R.; Iglesia, E. The Roles of Entropy and Enthalpy in Stabilizing Ion-Pairs at Transition States in Zeolite Acid Catalysis. *Acc. Chem. Res.* **2012**, *45* (2), 229–238.
- (9) Gounder, R.; Iglesia, E. The Catalytic Diversity of Zeolites: Confinement and Solvation Effects within Voids of Molecular Dimensions. *Chem. Commun.* **2013**, *49* (34), 3491–3509.
- (10) Loewenstein, W. The Distribution of Aluminum in the Tetrahedra of Silicates and Aluminates. *Am. Mineral.* **1954**, *39* (1–2), 92–96.
- (11) Sierka, M.; Eichler, U.; Datka, J.; Sauer, J. Heterogeneity of Brønsted Acidic Sites in Faujasite Type Zeolites Due to Aluminum Content and Framework Structure. *J. Phys. Chem. B* **1998**, *102* (33), 6397–6404.
- (12) Nystrom, S.; Hoffman, A.; Hibbitts, D. Tuning Brønsted Acid Strength by Altering Site Proximity in CHA Framework Zeolites. *ACS Catal.* **2018**, *8* (9), 7842–7860.

- (13) Hoffman, A. J.; Bates, J. S.; Di Iorio, J. R.; Nystrom, S. V.; Nimlos, C. T.; Gounder, R.; Hibbitts, D. Rigid Arrangements of Ionic Charge in Zeolite Frameworks Conferred by Specific Al Distributions Preferentially Stabilize Alkanol Dehydration Transition States. *Angew. Chem., Int. Ed.* **2020**, *59*, 18686.
- (14) Song, C.; Chu, Y.; Wang, M.; Shi, H.; Zhao, L.; Guo, X.; Yang, W.; Shen, J.; Xue, N.; Peng, L.; Ding, W. Cooperativity of Adjacent Brønsted Acid Sites in MFI Zeolite Channel Leads to Enhanced Polarization and Cracking of Alkanes. *J. Catal.* **2017**, *349*, 163–174.
- (15) Bernauer, M.; Tabor, E.; Pashkova, V.; Kaucký, D.; Sobalík, Z.; Wichterlová, B.; Dedecek, J. Proton Proximity – New Key Parameter Controlling Adsorption, Desorption and Activity in Propene Oligomerization over H-ZSM-5 Zeolites. *J. Catal.* **2016**, *344*, 157–172.
- (16) Tabor, E.; Bernauer, M.; Wichterlová, B.; Dedecek, J. Enhancement of Propene Oligomerization and Aromatization by Proximate Protons in Zeolites; FTIR Study of the Reaction Pathway in ZSM-5. *Catal. Sci. Technol.* **2019**, *9* (16), 4262–4275.
- (17) Sazama, P.; Dědeček, J.; Gábová, V.; Wichterlová, B.; Spoto, G.; Bordiga, S. Effect of Aluminium Distribution in the Framework of ZSM-5 on Hydrocarbon Transformation. Cracking of 1-Butene. *J. Catal.* **2008**, *254* (2), 180–189.
- (18) Chen, K.; Abdollahmani, M.; Horstmeier, S.; Pham, T. N.; Nguyen, V. T.; Zeets, M.; Wang, B.; Crossley, S.; White, J. L. Brønsted–Brønsted Synergies between Framework and Noncrystalline Protons in Zeolite H-ZSM-5. *ACS Catal.* **2019**, *9* (7), 6124–6136.
- (19) Zhou, Y.; Liu, H.; Rao, X.; Yue, Y.; Zhu, H.; Bao, X. Controlled Synthesis of ZSM-5 Zeolite with an Unusual Al Distribution in Framework from Natural Aluminosilicate Mineral. *Microporous Mesoporous Mater.* **2020**, *305*, 110357.
- (20) Nastase, S. A. F.; Cnudde, P.; Vanduyfhuys, L.; De Wispelaere, K.; Van Speybroeck, V.; Catlow, C. R. A.; Logsdail, A. J. Mechanistic Insight into the Framework Methylation of H-ZSM-5 for Varying Methanol Loading and Si/Al Ratio Using First Principles Molecular Dynamics Simulations. *ACS Catal.* **2020**, *10* (15), 8904–8915.
- (21) Giordanino, F.; Vennestrøm, P. N. R.; Lundegaard, L. F.; Stappen, F. N.; Mossin, S.; Beato, P.; Bordiga, S.; Lamberti, C. Characterization of Cu-Exchanged SSZ-13: A Comparative FTIR, UV-Vis, and EPR Study with Cu-ZSM-5 and Cu- $\beta$  with Similar Si/Al and Cu/Al Ratios. *Dalton Trans.* **2013**, *42* (35), 12741–12761.
- (22) Groothaert, M. H.; Lievens, K.; van Bokhoven, J. A.; Battiston, A. A.; Weckhuysen, B. M.; Pierloot, K.; Schoonheydt, R. A. Bis( $\mu$ -Oxo)Dicopper as Intermediate in the Catalytic Decomposition of NO over Cu-ZSM-5. In *Studies in Surface Science and Catalysis*; van Steen, E., Claeys, M., Callanan, L. H., Eds.; Elsevier: Amsterdam, 2004; Vol. 154, pp 2449–2457.
- (23) Paolucci, C.; Parekh, A. A.; Khurana, I.; Di Iorio, J. R.; Li, H.; Albarracín Caballero, J. D.; Shih, A. J.; Anggara, T.; Delgass, W. N.; Miller, J. T.; Ribeiro, F. H.; Gounder, R.; Schneider, W. F. Catalysis in a Cage: Condition-Dependent Speciation and Dynamics of Exchanged Cu Cations in SSZ-13 Zeolites. *J. Am. Chem. Soc.* **2016**, *138* (18), 6028–6048.
- (24) Sklenak, S.; Andrikopoulos, P. C.; Boekfa, B.; Jansang, B.; Nováková, J.; Benco, L.; Bucko, T.; Hafner, J.; Dědeček, J.; Sobalík, Z. N<sub>2</sub>O Decomposition over Fe-Zeolites: Structure of the Active Sites and the Origin of the Distinct Reactivity of Fe-Ferrierite, Fe-ZSM-5, and Fe-Beta. A Combined Periodic DFT and Multispectral Study. *J. Catal.* **2010**, *272* (2), 262–274.
- (25) Hansen, N.; Heyden, A.; Bell, A. T.; Keil, F. J. A Reaction Mechanism for the Nitrous Oxide Decomposition on Binuclear Oxygen Bridged Iron Sites in Fe-ZSM-5. *J. Phys. Chem. C* **2007**, *111* (5), 2092–2101.
- (26) Sobalík, Z.; Sazama, P.; Dedecek, J.; Wichterlová, B. Critical Evaluation of the Role of the Distribution of Al Atoms in the Framework for the Activity of Metallo-Zeolites in Redox N<sub>2</sub>O/NOx Reactions. *Appl. Catal., A* **2014**, *474*, 178–185.
- (27) Sazama, P.; Wichterlová, B.; Tabor, E.; Štátný, P.; Sathu, N. K.; Sobalík, Z.; Dědeček, J.; Sklenák, S.; Klein, P.; Vondrová, A. Tailoring of the Structure of Fe-Cationic Species in Fe-ZSM-5 by Distribution of Al Atoms in the Framework for N<sub>2</sub>O Decomposition and NH<sub>3</sub>-SCR-NOx. *J. Catal.* **2014**, *312*, 123–138.
- (28) Smeets, P. J.; Groothaert, M. H.; Schoonheydt, R. A. Cu Based Zeolites: A UV–Vis Study of the Active Site in the Selective Methane Oxidation at Low Temperatures. *Catal. Today* **2005**, *110* (3), 303–309.
- (29) Wulfers, M. J.; Teketel, S.; Ipek, B.; Lobo, R. F. Conversion of Methane to Methanol on Copper-Containing Small-Pore Zeolites and Zeotypes. *Chem. Commun.* **2015**, *51* (21), 4447–4450.
- (30) Devos, J.; Bols, M. L.; Plessers, D.; Goethem, C. V.; Seo, J. W.; Hwang, S.-J.; Sels, B. F.; Dusselier, M. Synthesis–Structure–Activity Relations in Fe-CHA for C–H Activation: Control of Al Distribution by Interzeolite Conversion. *Chem. Mater.* **2020**, *32* (1), 273–285.
- (31) Li, S.; Wang, Y.; Wu, T.; Schneider, W. F. First-Principles Analysis of Site- and Condition-Dependent Fe Speciation in SSZ-13 and Implications for Catalyst Optimization. *ACS Catal.* **2018**, *8* (11), 10119–10130.
- (32) Phadke, N. M.; Van der Mynsbrugge, J.; Mansoor, E.; Getsoian, A. B.; Head-Gordon, M.; Bell, A. T. Characterization of Isolated Ga<sup>3+</sup> Cations in Ga/H-MFI Prepared by Vapor-Phase Exchange of H-MFI Zeolite with GaCl<sub>3</sub>. *ACS Catal.* **2018**, *8* (7), 6106–6126.
- (33) Phadke, N. M.; Mansoor, E.; Bondil, M.; Head-Gordon, M.; Bell, A. T. Mechanism and Kinetics of Propane Dehydrogenation and Cracking over Ga/H-MFI Prepared via Vapor-Phase Exchange of H-MFI with GaCl<sub>3</sub>. *J. Am. Chem. Soc.* **2019**, *141* (4), 1614–1627.
- (34) Schreiber, M. W.; Plaisance, C. P.; Baumgärtl, M.; Reuter, K.; Jentys, A.; Bermejo-Deval, R.; Lercher, J. A. Lewis–Brønsted Acid Pairs in Ga/H-ZSM-5 To Catalyze Dehydrogenation of Light Alkanes. *J. Am. Chem. Soc.* **2018**, *140* (14), 4849–4859.
- (35) Gao, J.; Zheng, Y.; Jehng, J.-M.; Tang, Y.; Wachs, I. E.; Podkolzin, S. G. Identification of Molybdenum Oxide Nanostructures on Zeolites for Natural Gas Conversion. *Science* **2015**, *348* (6235), 686–690.
- (36) Gao, J.; Zheng, Y.; Fitzgerald, G. B.; de Joannis, J.; Tang, Y.; Wachs, I. E.; Podkolzin, S. G. Structure of Mo<sub>2</sub>Cx and Mo<sub>4</sub>Cx Molybdenum Carbide Nanoparticles and Their Anchoring Sites on ZSM-5 Zeolites. *J. Phys. Chem. C* **2014**, *118* (9), 4670–4679.
- (37) Razdan, N. K.; Kumar, A.; Foley, B. L.; Bhan, A. Influence of Ethylene and Acetylene on the Rate and Reversibility of Methane Dehydroaromatization on Mo/H-ZSM-5 Catalysts. *J. Catal.* **2020**, *381*, 261–270.
- (38) Pinilla-Herrero, I.; Borfecchia, E.; Holzinger, J.; Mentzel, U. V.; Joensen, F.; Lomachenko, K. A.; Bordiga, S.; Lamberti, C.; Berlier, G.; Olsbye, U.; Svelle, S.; Skibsted, J.; Beato, P. High Zn/Al Ratios Enhance Dehydrogenation vs Hydrogen Transfer Reactions of Zn-ZSM-5 Catalytic Systems in Methanol Conversion to Aromatics. *J. Catal.* **2018**, *362*, 146–163.
- (39) Findley, J. M.; Ravikovitch, P. I.; Sholl, D. S. The Effect of Aluminum Short-Range Ordering on Carbon Dioxide Adsorption in Zeolites. *J. Phys. Chem. C* **2018**, *122* (23), 12332–12340.
- (40) Yang, C.-T.; Janda, A.; Bell, A. T.; Lin, L.-C. Atomistic Investigations of the Effects of Si/Al Ratio and Al Distribution on the Adsorption Selectivity of n-Alkanes in Brønsted-Acid Zeolites. *J. Phys. Chem. C* **2018**, *122* (17), 9397–9410.
- (41) Zeets, M.; Resasco, D. E.; Wang, B. Enhanced Chemical Activity and Wettability at Adjacent Brønsted Acid Sites in HZSM-5. *Catal. Today* **2018**, *312*, 44–50.
- (42) Prodingler, S.; Derewinski, M. A.; Wang, Y.; Washton, N. M.; Walter, E. D.; Szanyi, J.; Gao, F.; Wang, Y.; Peden, C. H. F. Submicron Cu/SSZ-13: Synthesis and Application as Selective Catalytic Reduction (SCR) Catalysts. *Appl. Catal., B* **2017**, *201*, 461–469.
- (43) Kim, Y. J.; Lee, J. K.; Min, K. M.; Hong, S. B.; Nam, I.-S.; Cho, B. K. Hydrothermal Stability of CuSSZ13 for Reducing NOx by NH<sub>3</sub>. *J. Catal.* **2014**, *311*, 447–457.
- (44) Dusselier, M.; Deimund, M. A.; Schmidt, J. E.; Davis, M. E. Methanol-to-Olefins Catalysis with Hydrothermally Treated Zeolite SSZ-39. *ACS Catal.* **2015**, *5* (10), 6078–6085.

- (45) Pashkova, V.; Klein, P.; Dedecek, J.; Tokarová, V.; Wichterlová, B. Incorporation of Al at ZSM-5 Hydrothermal Synthesis. Tuning of Al Pairs in the Framework. *Microporous Mesoporous Mater.* **2015**, *202*, 138–146.
- (46) Yokoi, T.; Mochizuki, H.; Namba, S.; Kondo, J. N.; Tatsumi, T. Control of the Al Distribution in the Framework of ZSM-5 Zeolite and Its Evaluation by Solid-State NMR Technique and Catalytic Properties. *J. Phys. Chem. C* **2015**, *119* (27), 15303–15315.
- (47) Yokoi, T.; Mochizuki, H.; Biligetu, T.; Wang, Y.; Tatsumi, T. Unique Al Distribution in the MFI Framework and Its Impact on Catalytic Properties. *Chem. Lett.* **2017**, *46* (6), 798–800.
- (48) Biligetu, T.; Wang, Y.; Nishitoba, T.; Otomo, R.; Park, S.; Mochizuki, H.; Kondo, J. N.; Tatsumi, T.; Yokoi, T. Al Distribution and Catalytic Performance of ZSM-5 Zeolites Synthesized with Various Alcohols. *J. Catal.* **2017**, *353*, 1–10.
- (49) Chawla, A.; Li, R.; Jain, R.; Clark, R. J.; Sutjianto, J. G.; Palmer, J. C.; Rimer, J. D. Cooperative Effects of Inorganic and Organic Structure-Directing Agents in ZSM-5 Crystallization. *Mol. Syst. Des. Eng.* **2018**, *3* (1), 159–170.
- (50) Dedecek, J.; Balgová, V.; Pashkova, V.; Klein, P.; Wichterlová, B. Synthesis of ZSM-5 Zeolites with Defined Distribution of Al Atoms in the Framework and Multinuclear MAS NMR Analysis of the Control of Al Distribution. *Chem. Mater.* **2012**, *24* (16), 3231–3239.
- (51) Di Iorio, J. R.; Nimlos, C. T.; Gounder, R. Introducing Catalytic Diversity into Single-Site Chabazite Zeolites of Fixed Composition via Synthetic Control of Active Site Proximity. *ACS Catal.* **2017**, *7* (10), 6663–6674.
- (52) Di Iorio, J. R.; Li, S.; Jones, C. B.; Nimlos, C. T.; Wang, Y.; Kunkes, E.; Vattipalli, V.; Prasad, S.; Moini, A.; Schneider, W. F.; Gounder, R. Cooperative and Competitive Occlusion of Organic and Inorganic Structure-Directing Agents within Chabazite Zeolites Influences Their Aluminum Arrangement. *J. Am. Chem. Soc.* **2020**, *142* (10), 4807–4819.
- (53) Dědeček, J.; Kaucký, D.; Wichterlová, B. Co<sup>2+</sup> Ion Siting in Pentasil-Containing Zeolites, Part 3: Co<sup>2+</sup> Ion Sites and Their Occupation in ZSM-5: A VIS Diffuse Reflectance Spectroscopy Study. *Microporous Mesoporous Mater.* **2000**, *35–36*, 483–494.
- (54) Dědeček, J.; Kaucký, D.; Wichterlová, B.; Gonsiorová, O. Co<sup>2+</sup> Ions as Probes of Al Distribution in the Framework of Zeolites. ZSM-5 Study. *Phys. Chem. Chem. Phys.* **2002**, *4* (21), 5406–5413.
- (55) Janda, A.; Bell, A. T. Effects of Si/Al Ratio on the Distribution of Framework Al and on the Rates of Alkane Monomolecular Cracking and Dehydrogenation in H-MFI. *J. Am. Chem. Soc.* **2013**, *135* (51), 19193–19207.
- (56) Drozdová, L.; Prins, R.; Dědeček, J.; Sobalík, Z.; Wichterlová, B. Bonding of Co Ions in ZSM-5, Ferrierite, and Mordenite: An X-Ray Absorption, UV–Vis, and IR Study. *J. Phys. Chem. B* **2002**, *106* (9), 2240–2248.
- (57) Li, C.; Vidal-Moya, A.; Miguel, P. J.; Dedecek, J.; Boronat, M.; Corma, A. Selective Introduction of Acid Sites in Different Confined Positions in ZSM-5 and Its Catalytic Implications. *ACS Catal.* **2018**, *8* (8), 7688–7697.
- (58) Hur, Y. G.; Kester, P. M.; Nimlos, C. T.; Cho, Y.; Miller, J. T.; Gounder, R. Influence of Tetrapropylammonium and Ethylenediamine Structure-Directing Agents on the Framework Al Distribution in B–Al–MFI Zeolites. *Ind. Eng. Chem. Res.* **2019**, *58* (27), 11849–11860.
- (59) Chupin, C.; van Veen, A. C.; Konduru, M.; Després, J.; Mirodatos, C. Identity and Location of Active Species for NO Reduction by CH<sub>4</sub> over Co-ZSM-5. *J. Catal.* **2006**, *241* (1), 103–114.
- (60) Desai, A. J.; Kovalchuk, V. I.; Lombardo, E. A.; d'Itri, J. L. CoZSM-5: Why This Catalyst Selectively Reduces NO<sub>x</sub> with Methane. *J. Catal.* **1999**, *184* (2), 396–405.
- (61) Kaucký, D.; Vondrová, A.; Dědeček, J.; Wichterlová, B. Activity of Co Ion Sites in ZSM-5, Ferrierite, and Mordenite in Selective Catalytic Reduction of NO with Methane. *J. Catal.* **2000**, *194* (2), 318–329.
- (62) Li, H.; Paolucci, C.; Khurana, I.; Wilcox, L. N.; Goltl, F.; Albarracín-Caballero, J. D.; Shih, A. J.; Ribeiro, F. H.; Gounder, R.; Schneider, W. F. Consequences of Exchange-Site Heterogeneity and Dynamics on the UV-Visible Spectrum of Cu-Exchanged SSZ-13. *Chem. Sci.* **2019**, *10* (8), 2373–2384.
- (63) Liotta, L. F.; Pantaleo, G.; Macaluso, A.; Di Carlo, G.; Deganello, G. CoO<sub>x</sub> Catalysts Supported on Alumina and Alumina-Baria: Influence of the Support on the Cobalt Species and Their Activity in NO Reduction by C<sub>3</sub>H<sub>6</sub> in Lean Conditions. *Appl. Catal., A* **2003**, *245* (1), 167–177.
- (64) Radovanovic, P. V.; Norberg, N. S.; McNally, K. E.; Gamelin, D. R. Colloidal Transition-Metal-Doped ZnO Quantum Dots. *J. Am. Chem. Soc.* **2002**, *124* (51), 15192–15193.
- (65) Bellmann, A.; Rautenberg, C.; Benstrup, U.; Brückner, A. Determining the Location of Co<sup>2+</sup> in Zeolites by UV-Vis Diffuse Reflection Spectroscopy: A Critical View. *Catalysts* **2020**, *10* (1), 123.
- (66) Dědeček, J.; Tabor, E.; Sklenak, S. Tuning the Aluminum Distribution in Zeolites to Increase Their Performance in Acid-Catalyzed Reactions. *ChemSusChem* **2019**, *12* (3), 556–576.
- (67) Di Iorio, J. R.; Gounder, R. Controlling the Isolation and Pairing of Aluminum in Chabazite Zeolites Using Mixtures of Organic and Inorganic Structure-Directing Agents. *Chem. Mater.* **2016**, *28* (7), 2236–2247.
- (68) Park, S.; Biligetu, T.; Wang, Y.; Nishitoba, T.; Kondo, J. N.; Yokoi, T. Acidic and Catalytic Properties of ZSM-5 Zeolites with Different Al Distributions. *Catal. Today* **2018**, *303*, 64–70.
- (69) Kallus, S.; Patarin, J.; Caulet, P.; Faust, A. C. Synthesis of Boron-Beta Zeolite from near-Neutral Fluoride-Containing Gels. *Microporous Mater.* **1997**, *10* (4), 181–188.
- (70) Caulet, P.; Hazm, J.; Guth, J. L.; Joly, J. F.; Lynch, J.; Raatz, F. Synthesis of Zeolite Beta from Nonalkaline Fluoride Aqueous Aluminosilicate Gels. *Zeolites* **1992**, *12* (3), 240–250.
- (71) Bates, S. A.; Delgass, W. N.; Ribeiro, F. H.; Miller, J. T.; Gounder, R. Methods for NH<sub>3</sub> Titration of Brønsted Acid Sites in Cu-Zeolites That Catalyze the Selective Catalytic Reduction of NO<sub>x</sub> with NH<sub>3</sub>. *J. Catal.* **2014**, *312*, 26–36.
- (72) Di Iorio, J. R.; Bates, S. A.; Verma, A. A.; Delgass, W. N.; Ribeiro, F. H.; Miller, J. T.; Gounder, R. The Dynamic Nature of Brønsted Acid Sites in Cu–Zeolites During NO<sub>x</sub> Selective Catalytic Reduction: Quantification by Gas-Phase Ammonia Titration. *Top. Catal.* **2015**, *58* (7), 424–434.
- (73) Kresse, G.; Furthmüller, J. Efficiency of Ab-Initio Total Energy Calculations for Metals and Semiconductors Using a Plane-Wave Basis Set. *Comput. Mater. Sci.* **1996**, *6* (1), 15–50.
- (74) Kresse, G.; Furthmüller, J. Efficient Iterative Schemes for Ab Initio Total-Energy Calculations Using a Plane-Wave Basis Set. *Phys. Rev. B: Condens. Matter Mater. Phys.* **1996**, *54* (16), 11169–11186.
- (75) Kresse, G.; Hafner, J. Norm-Conserving and Ultrasoft Pseudopotentials for First-Row and Transition Elements. *J. Phys.: Condens. Matter* **1994**, *6* (40), 8245–8257.
- (76) Kresse, G.; Hafner, J. Ab Initio Molecular Dynamics for Liquid Metals. *Phys. Rev. B: Condens. Matter Mater. Phys.* **1993**, *47* (1), 558–561.
- (77) Kravchenko, P.; Plaisance, C.; Hibbitts, D. A New Computational Interface for Catalysis. 2019, ChemRxiv; [https://chemrxiv.org/articles/preprint/A\\_New\\_Computational\\_Interface\\_for\\_Catalysis/8040737](https://chemrxiv.org/articles/preprint/A_New_Computational_Interface_for_Catalysis/8040737) (accessed Jul 31, 2020).
- (78) Blöchl, P. E. Projector Augmented-Wave Method. *Phys. Rev. B: Condens. Matter Mater. Phys.* **1994**, *50* (24), 17953–17979.
- (79) Kresse, G.; Joubert, D. From Ultrasoft Pseudopotentials to the Projector Augmented-Wave Method. *Phys. Rev. B: Condens. Matter Mater. Phys.* **1999**, *59* (3), 1758–1775.
- (80) Perdew, J. P.; Burke, K.; Ernzerhof, M. Generalized Gradient Approximation Made Simple. *Phys. Rev. Lett.* **1996**, *77* (18), 3865–3868.
- (81) Grimme, S.; Antony, J.; Ehrlich, S.; Krieg, H. A Consistent and Accurate Ab Initio Parametrization of Density Functional Dispersion Correction (DFT-D) for the 94 Elements H–Pu. *J. Chem. Phys.* **2010**, *132* (15), 154104.

- (82) Grimme, S.; Ehrlich, S.; Goerigk, L. Effect of the Damping Function in Dispersion Corrected Density Functional Theory. *J. Comput. Chem.* **2011**, *32* (7), 1456–1465.
- (83) Mathew, K.; Sundararaman, R.; Letchworth-Weaver, K.; Arias, T. A.; Hennig, R. G. Implicit Solvation Model for Density-Functional Study of Nanocrystal Surfaces and Reaction Pathways. *J. Chem. Phys.* **2014**, *140* (8), 084106.
- (84) Archer, D. G.; Wang, P. The Dielectric Constant of Water and Debye-Hückel Limiting Law Slopes. *J. Phys. Chem. Ref. Data* **1990**, *19* (2), 371–411.
- (85) van Koningsveld, H. High-Temperature (350 K) Orthorhombic Framework Structure of Zeolite H-ZSM-5. *Acta Crystallogr., Sect. B: Struct. Sci.* **1990**, *46* (6), 731–735.
- (86) Hoffman, A.; DeLuca, M.; Hibbitts, D. Restructuring of MFI Framework Zeolite Models and Their Associated Artifacts in Density Functional Theory Calculations. *J. Phys. Chem. C* **2019**, *123* (11), 6572–6585.
- (87) Yokomori, Y.; Idaka, S. The Structure of TPA-ZSM-5 with Si/Al = 23. *Microporous Mesoporous Mater.* **1999**, *28* (3), 405–413.
- (88) Sierka, M.; Sauer, J. Proton Mobility in Chabazite, Faujasite, and ZSM-5 Zeolite Catalysts. Comparison Based on Ab Initio Calculations. *J. Phys. Chem. B* **2001**, *105* (8), 1603–1613.
- (89) Ryder, J. A.; Chakraborty, A. K.; Bell, A. T. Density Functional Theory Study of Proton Mobility in Zeolites: Proton Migration and Hydrogen Exchange in ZSM-5. *J. Phys. Chem. B* **2000**, *104* (30), 6998–7011.
- (90) Tuma, C.; Sauer, J. A Hybrid MP2/Planewave-DFT Scheme for Large Chemical Systems: Proton Jumps in Zeolites. *Chem. Phys. Lett.* **2004**, *387* (4), 388–394.
- (91) Gounder, R.; Jones, A. J.; Carr, R. T.; Iglesia, E. Solvation and Acid Strength Effects on Catalysis by Faujasite Zeolites. *J. Catal.* **2012**, *286*, 214–223.
- (92) Ewald, P. P. Die Berechnung Optischer Und Elektrostatischer Gitterpotentiale. *Ann. Phys.* **1921**, *369* (3), 253–287.
- (93) Gale, J. D. GULP: A Computer Program for the Symmetry-Adapted Simulation of Solids. *J. Chem. Soc., Faraday Trans.* **1997**, *93* (4), 629–637.
- (94) Gale, J. D.; Rohl, A. L. The General Utility Lattice Program (GULP). *Mol. Simul.* **2003**, *29* (5), 291–341.
- (95) Jones, A. J.; Carr, R. T.; Zones, S. I.; Iglesia, E. Acid Strength and Solvation in Catalysis by MFI Zeolites and Effects of the Identity, Concentration and Location of Framework Heteroatoms. *J. Catal.* **2014**, *312*, 58–68.
- (96) van Bokhoven, J. A.; Sambe, H.; Ramaker, D. E.; Koningsberger, D. C. Al K-Edge Near-Edge X-Ray Absorption Fine Structure (NEXAFS) Study on the Coordination Structure of Aluminum in Minerals and Y Zeolites. *J. Phys. Chem. B* **1999**, *103* (36), 7557–7564.
- (97) van Bokhoven, J. A.; van der Eerden, A. M. J.; Koningsberger, D. C. Three-Coordinate Aluminum in Zeolites Observed with In Situ X-Ray Absorption Near-Edge Spectroscopy at the Al K-Edge: Flexibility of Aluminum Coordinations in Zeolites. *J. Am. Chem. Soc.* **2003**, *125* (24), 7435–7442.
- (98) Omegna, A.; van Bokhoven, J. A.; Prins, R. Flexible Aluminum Coordination in Alumino-Silicates. Structure of Zeolite H-USY and Amorphous Silica-Alumina. *J. Phys. Chem. B* **2003**, *107* (34), 8854–8860.
- (99) Ravi, M.; Sushkevich, V. L.; van Bokhoven, J. A. Lewis Acidity Inherent to the Framework of Zeolite Mordenite. *J. Phys. Chem. C* **2019**, *123* (24), 15139–15144.
- (100) Kraus, H.; Müller, M.; Prins, R.; Kentgens, A. P. M. Comments on the 27Al NMR Visibility of Aluminas. *J. Phys. Chem. B* **1998**, *102* (20), 3862–3865.
- (101) Parker, L. M.; Bibby, D. M.; Patterson, J. E. Thermal Decomposition of ZSM-5 and Silicalite Precursors. *Zeolites* **1984**, *4* (2), 168–174.
- (102) Chao, K.-J.; Lin, J.-C.; Wang, Y.; Lee, G. H. Single Crystal Structure Refinement of TPA ZSM-5 Zeolite. *Zeolites* **1986**, *6* (1), 35–38.
- (103) Burkett, S. L.; Davis, M. E. Mechanisms of Structure Direction in the Synthesis of Pure-Silica Zeolites. 1. Synthesis of TPA/Si-ZSM-5. *Chem. Mater.* **1995**, *7* (5), 920–928.
- (104) Burkett, S. L.; Davis, M. E. Mechanism of Structure Direction in the Synthesis of Si-ZSM-5: An Investigation by Intermolecular  $^1\text{H}$ - $^{29}\text{Si}$  CP MAS NMR. *J. Phys. Chem.* **1994**, *98* (17), 4647–4653.
- (105) Chang, C. D.; Bell, A. T. Studies on the Mechanism of ZSM-5 Formation. *Catal. Lett.* **1991**, *8* (5), 305–316.
- (106) Park, M. B.; Lee, Y.; Zheng, A.; Xiao, F.-S.; Nicholas, C. P.; Lewis, G. J.; Hong, S. B. Formation Pathway for LTA Zeolite Crystals Synthesized via a Charge Density Mismatch Approach. *J. Am. Chem. Soc.* **2013**, *135* (6), 2248–2255.
- (107) Lewis, G. J.; Miller, M. A.; Moscoso, J. G.; Wilson, B. A.; Knight, L. M.; Wilson, S. T. Experimental Charge Density Matching Approach to Zeolite Synthesis. In *Studies in Surface Science and Catalysis*; van Steen, E., Claeys, I. M., Callanan, L. H., Eds.; Elsevier: Amsterdam, 2004; Vol. 154, pp 364–372.
- (108) Kim, S. H.; Park, M. B.; Min, H.-K.; Hong, S. B. Zeolite Synthesis in the Tetraethylammonium–Tetramethylammonium Mixed-Organic Additive System. *Microporous Mesoporous Mater.* **2009**, *123* (1), 160–168.
- (109) Miller, M. A.; Lewis, G. J.; Moscoso, J. G.; Koster, S.; Modica, F.; Gatter, M. G.; Nemeth, L. T. Synthesis and Catalytic Activity of UZM-12. In *Studies in Surface Science and Catalysis*; Xu, R., Gao, Z., Chen, J., Yan, W., Eds.; Elsevier: Amsterdam, 2007; Vol. 170, pp 487–492.
- (110) Miller, M. A.; Moscoso, J. G.; Koster, S. C.; Gatter, M. G.; Lewis, G. J. Synthesis and Characterization of the 12-Ring Zeolites UZM-4 (BPH) and UZM-22 (MEI) via the Charge Density Mismatch Approach in the Choline-Li<sub>2</sub>O-SrO-Al<sub>2</sub>O<sub>3</sub>-SiO<sub>2</sub> System. In *Studies in Surface Science and Catalysis*; Elsevier: Amsterdam, 2007; Vol. 170, pp 347–354.
- (111) Blackwell, C. S.; Broach, R. W.; Gatter, M. G.; Holmgren, J. S.; Jan, D.-Y.; Lewis, G. J.; Mezza, B. J.; Mezza, T. M.; Miller, M. A.; Moscoso, J. G.; Patton, R. L.; Rohde, L. M.; Schoonover, M. W.; Sinkler, W.; Wilson, B. A.; Wilson, S. T. Open-Framework Materials Synthesized in the TMA+/TEA+ Mixed-Template System: The New Low Si/Al Ratio Zeolites UZM-4 and UZM-5. *Angew. Chem., Int. Ed.* **2003**, *42* (15), 1737–1740.
- (112) Nakamoto, H.; Takahashi, H. Crystallization of Zeolite ZSM-5 from Single Cation System. *Chem. Lett.* **1981**, *10* (12), 1739–1742.
- (113) Qin, W.; Zhou, Y.; Rimer, J. D. Deleterious Effects of Non-Framework Al Species on the Catalytic Performance of ZSM-5 Crystals Synthesized at Low Temperature. *React. Chem. Eng.* **2019**, *4* (11), 1957–1968.
- (114) Shantz, D. F.; Schmedt auf der Günne, J.; Koller, H.; Lobo, R. F. Multiple-Quantum  $^1\text{H}$  MAS NMR Studies of Defect Sites in As-Made All-Silica ZSM-12 Zeolite. *J. Am. Chem. Soc.* **2000**, *122* (28), 6659–6663.
- (115) Ghorbanpour, A.; Rimer, J. D.; Grabow, L. C. Periodic, VdW-Corrected Density Functional Theory Investigation of the Effect of Al Siting in H-ZSM-5 on Chemisorption Properties and Site-Specific Acidity. *Catal. Commun.* **2014**, *52*, 98–102.
- (116) Derouane, E. G.; Fripiat, J. G. Non-Empirical Quantum Chemical Study of the Siting and Pairing of Aluminium in the MFI Framework. *Zeolites* **1985**, *5* (3), 165–172.
- (117) Lonsinger, S. R.; Chakraborty, A. K.; Theodorou, D. N.; Bell, A. T. The Effects of Local Structural Relaxation on Aluminum Siting within H-ZSM-5. *Catal. Lett.* **1991**, *11* (2), 209–217.
- (118) Alvarado-Swaigood, A. E.; Barr, M. K.; Hay, P. J.; Redondo, A. Ab Initio Quantum Chemical Calculations of Aluminum Substitution in Zeolite ZSM-5. *J. Phys. Chem.* **1991**, *95* (24), 10031–10036.
- (119) Li, S.; Gounder, R.; Debellis, A.; Müller, I. B.; Prasad, S.; Moini, A.; Schneider, W. F. Influence of the N,N,N-Trimethyl-1-Adamantyl Ammonium Structure-Directing Agent on Al Substitution in SSZ-13 Zeolite. *J. Phys. Chem. C* **2019**, *123* (28), 17454–17458.

- (120) Goodman, B. R.; Hass, K. C.; Schneider, W. F.; Adams, J. B. Statistical Analysis of Al Distributions and Metal Ion Pairing Probabilities in Zeolites. *Catal. Lett.* **2000**, *68* (1), 85–93.
- (121) Mlekodaj, K.; Dedecek, J.; Pashkova, V.; Tabor, E.; Klein, P.; Urbanova, M.; Karcz, R.; Sazama, P.; Whittleton, S. R.; Thomas, H. M.; Fishchuk, A. V.; Sklenak, S. Al Organization in the SSZ-13 Zeolite. Al Distribution and Extraframework Sites of Divalent Cations. *J. Phys. Chem. C* **2019**, *123* (13), 7968–7987.
- (122) Li, S.; Li, H.; Gounder, R.; Debellis, A.; Müller, I. B.; Prasad, S.; Moini, A.; Schneider, W. F. First-Principles Comparison of Proton and Divalent Copper Cation Exchange Energy Landscapes in SSZ-13 Zeolite. *J. Phys. Chem. C* **2018**, *122* (41), 23564–23573.
- (123) Kim, S. D.; Noh, S. H.; Park, J. W.; Kim, W. J. Organic-Free Synthesis of ZSM-5 with Narrow Crystal Size Distribution Using Two-Step Temperature Process. *Microporous Mesoporous Mater.* **2006**, *92* (1), 181–188.
- (124) Kim, S. D.; Noh, S. H.; Seong, K. H.; Kim, W. J. Compositional and Kinetic Study on the Rapid Crystallization of ZSM-5 in the Absence of Organic Template under Stirring. *Microporous Mesoporous Mater.* **2004**, *72* (1), 185–192.
- (125) Hedlund, J.; Noack, M.; Kölsch, P.; Creaser, D.; Caro, J.; Sterte, J. ZSM-5 Membranes Synthesized without Organic Templates Using a Seeding Technique. *J. Membr. Sci.* **1999**, *159* (1), 263–273.
- (126) Olson, D. H.; Haag, W. O.; Lago, R. M. Chemical and Physical Properties of the ZSM-5 Substitutional Series. *J. Catal.* **1980**, *61* (2), 390–396.
- (127) Lok, B. M.; Cannan, T. R.; Messina, C. A. The Role of Organic Molecules in Molecular Sieve Synthesis. *Zeolites* **1983**, *3* (4), 282–291.
- (128) Takewaki, T.; Beck, L. W.; Davis, M. E. Zeolite Synthesis Using 1,4-Diazabicyclo[2,2,2]Octane (DABCO) Derivatives as Structure-Directing Agents. *Microporous Mesoporous Mater.* **1999**, *33* (1), 197–207.
- (129) Kubota, Y.; Honda, T.; Plévert, J.; Yamashita, T.; Okubo, T.; Sugi, Y. Synthesis of a New Molecular Sieve Using DABCO-Based Structure-Directing Agent. *Catal. Today* **2002**, *74* (3), 271–279.
- (130) Towns, J.; Cockerill, T.; Dahan, M.; Foster, I.; Gaither, K.; Grimshaw, A.; Hazlewood, V.; Lathrop, S.; Lifka, D.; Peterson, G. D.; Roskies, R.; Scott, J. R.; Wilkins-Diehr, N. XSEDE: Accelerating Scientific Discovery. *Comput. Sci. Eng.* **2014**, *16* (5), 62–74.